INTERNATIONAL JOURNAL FOR NUMERICAL METHODS IN FLUIDS
Int. J. Numer. Meth. Fluids 2006; **51**:385–424
Published online 20 December 2005 in Wiley InterScience (www.interscience.wiley.com). DOI: 10.1002/fld.1108

A consistent splitting scheme for unsteady incompressible viscous flows I. Dirichlet boundary condition and applications

J. C.-F. Wong[1,*,†] and M. K.-H. Chan[2,‡]

[1]*Department of Mathematics, Room 220, Lady Shaw Building, The Chinese University of Hong Kong, Shatin, Hong Kong*
[2]*School of Mathematical Sciences, University of Exeter, Laver Building, North Park Road, Exeter, EX4 4QE, U.K.*

SUMMARY

A well-recognized approach for handling the incompressibility constraint by operating directly on the discretized Navier–Stokes equations is used to obtain the decoupling of the pressure from the velocity field. By following the current developments by Guermond and Shen, the possibilities of obtaining accurate pressure and reducing boundary-layer effect for the pressure are analysed. The present study mainly reports the numerical solutions of an unsteady Navier–Stokes problem based on the so-called consistent splitting scheme (*J. Comput. Phys.* 2003; **192**:262–276). At the same time the Dirichlet boundary value conditions are considered. The accuracy of the method is carefully examined against the exact solution for an unsteady flow physics problem in a simply connected domain. The effectiveness is illustrated viz. several computations of 2D double lid-driven cavity problems. Copyright © 2005 John Wiley & Sons, Ltd.

KEY WORDS: Navier–Stokes equation; incompressible/viscous flow; consistent splitting method; mixed finite element; double lid-driven cavity

1. INTRODUCTION

Over the last 30 years, the fractional-step projection method (or the pressure correction method) developed by Chorin [1, 2] and Témam [3, 4] has been greatly proclaimed as an effective tool for solving unsteady incompressible viscous flow problems. The most attractive features of this method are its extreme simplicity and the robustness of the solutions of the decoupled velocity and pressure. Comprehensive reviews of different formulations and the

*Correspondence to: J. C.-F. Wong, Department of Mathematics, Room 220, Lady Shaw Building, The Chinese University of Hong Kong, Shatin, Hong Kong.
†E-mail: jwong@math.cuhk.edu.hk
‡E-mail: K.H.Chan@exeter.ac.uk

Received 4 May 2005
Revised 31 August 2005
Accepted 2 September 2005

results obtained are presented in References [5–9]. An overview of this latest development in unsteady incompressible viscous flow is given in Reference [10].

Recently, Guermond and Shen [11] introduced the consistent splitting scheme for solving unsteady flow problems. Three main characteristics are present in the scheme. One is the self-maintenance concept of the usual fractional-step projection method, such that the incompressibility constraint is directly satisfied by solving the Poisson problem for the pressure. Instead of determining the pressure, the auxiliary pressure is calculated. Another is the diminishment of the boundary-layer effect for the pressure, such that an extra divergence-free term derived from the viscosity term is included in the pressure Poisson equation in a weak sense. The last is that there is no need to determine an intermediate velocity.

A lot of work has been carried out on the theoretical justifications and numerical verifications of unsteady Navier–Stokes and Stokes problems [11–14] based on the crucial formulation of adding an extra divergence-free term for correcting the pressure. Still, there is a lack of practical investigation on the numerical performance of the scheme of the Navier–Stokes case. In this article, moderate Reynolds numbers for the double lid-driven cavity problem are studied and compared with other numerical results. Pan and Glowinski [15] (see also Reference [8] in detail) were among the few who solved the two-sided wall-driven cavity problem. Using the primitive variable formulation, they studied the parametric case of the critical Reynolds number that lies in between 4000 and 5000 when the regular grid of 256×256 is used and the time step-size is $\Delta t = 0.0005$. They concluded that a Hopf bifurcation and a break of symmetry would appear at $Re = 5000$ when long time simulations were made. The term 'double lid-driven cavity' problem was probably first introduced by Ben-Artzi *et al.* [16] who obtained the steady-state solution for the case with $Re = 10\,000$ and a 257×257 grid at $t \leqslant 45$ using the vorticity/stream-function formulation. They considered that the flow starts impulsively from zero. In a more recent paper by Ben-Artzi *et al.* [17], a break of symmetry was indicated for the double lid-driven cavity problem for Re falling into the range from 2000 to 3200. Up to the present time, it seems that a Hopf bifurcation does hold for this problem. Kupferman [18] obtained the steady-state solution for the case with $Re = 20\,000$ and a 128×128 grid at $t \leqslant 18$ using the vorticity/stream-function formulation. Based on the finite difference framework, the same investigator used the Kurganov and Tadmor central-difference scheme [19] for solving the advection term, the Altas *et al.* compact stencil [20] for solving the biharmonic viscous term and an algebraic multigrid solver [21] for solving the fourth-order elliptic equation.

In the present study, we report detailed numerical verifications of the mixed finite element consistent splitting scheme, and then study numerical simulations for the double lid-driven cavity by making use of two different mesh layouts. Using a fine grid mesh with 513×513 points, the double-lid driven cavity is solved for $Re = 10\,000$ with respect to the two different directions of the moving lids. The results for the evolution of a symmetric pair of vortical structures are obtained.

In Section 2, we review the governing equations of the unsteady incompressible viscous flows. We provide a brief description of the consistent splitting scheme in Section 3 and more detail on the concept of numerical implementation and discretization. The applications of the scheme and the computational test cases are illustrated and discussed in Section 4. In Section 5, we present our numerical examples, and end with concluding remarks in Section 6.

2. GOVERNING EQUATION

Let Ω be a bounded domain in Euclidean space $\mathbb{R}^2$ with a piecewise smooth boundary $\partial\Omega$. A fixed final time is denoted by T. We shall be concerned with the two-dimensional (2D) unsteady (transient or time-dependent) Navier–Stokes (NS) equation of incompressible viscous fluid in a dimensional form:

$$\frac{\partial \mathbf{u}}{\partial t} + \mathbf{u} \cdot \nabla \mathbf{u} = -\frac{1}{\rho}\nabla p + \nu \nabla^2 \mathbf{u} + \mathbf{f} \quad \text{in } \Omega \times (0, T] \tag{1}$$

with

$$\nabla \cdot \mathbf{u} = 0 \quad \text{in } \Omega \times [0, T] \tag{2}$$

where t is the time(s) and $\mathbf{x} = (x, y)$ is a function of 2D position in the Cartesian coördinate system; $\mathbf{u} = \mathbf{u}(\mathbf{x}, t)$, $p = p(\mathbf{x}, t)$, ρ and ν are the velocity vector, pressure, density and kinematic viscosity, respectively; $\mathbf{f} = (f_x, f_y)$ is the 2D given force vector; ∇, ∇^2 and $\nabla\cdot$ are the gradient, Laplacian and divergence operators, respectively. The spatial and temporal domain of a solution is denoted by $\Omega \times [0, T]$. Dirichlet boundary conditions on the velocity vector are:

$$\mathbf{u} = \mathbf{b}(\mathbf{x}, t) \quad \text{on } \partial\Omega \times [0, T] \tag{3}$$

with[§]

$$\int_{\partial\Omega} \mathbf{n} \cdot \mathbf{b} \, \mathrm{d}S = 0 \tag{4}$$

where $\mathbf{b}$ is a known velocity vector function on the entire boundary $\partial\Omega$ of Ω (or $\partial\Omega$ being the piecewise smooth boundary of Ω), and $\mathbf{n}$ is the outward-pointing normal vector on $\partial\Omega$. Initial conditions are:

$$\mathbf{u}(\mathbf{x}, t = 0) = \mathbf{u}_0(\mathbf{x}), \quad \mathbf{x} \in \bar{\Omega} \tag{5}$$

with[¶]

$$\nabla \cdot \mathbf{u}_0 = 0, \quad \mathbf{x} \in \bar{\Omega} \tag{6}$$

and

$$\mathbf{n} \cdot \mathbf{u}_0 = \mathbf{n} \cdot \mathbf{b}(\mathbf{x}, t = 0) \quad \text{on } \partial\Omega \tag{7}$$

where $\mathbf{u}_0$ is a prescribed velocity vector function and $\bar{\Omega} = \Omega \cup \partial\Omega$ will denote the closure of Ω. Note that if any of the three constraints on the input data, Equations (4), (6) and (7), are

[§]This expression is simply the divergence theorem, which is equivalent to a mass conservation law, stating that the total volume of all sinks and sources, i.e. the volume integral of the divergence, is equal to the net flow across the volume's boundary, i.e.

$$\int_{\Omega} \nabla \cdot \mathbf{b} \, \mathrm{d}\Omega = \int_{\partial\Omega} \mathbf{n} \cdot \mathbf{b} \, \mathrm{d}S = 0$$

[¶]This constraint is simply the incompressibility constraint, stating that the initial data must satisfy the divergence-free condition.

violated, the problem is ill-posed and no solution exists (see e.g. Reference [5]). In addition, the data are assumed to be regular enough and to satisfy all the compatibility conditions needed for a smooth solution to exist for all time (see e.g. Reference [22]).

Let us mention the crucial idea that the pressure is uniquely determined up to an additive constant. Problems of the form

$$\int_{\Omega} p(\mathbf{x},t)\,\mathrm{d}\Omega = 0 \tag{8}$$

with $p(\mathbf{x},t)+\mathrm{Const}$ can be considered as a variety of pressure solutions to the Navier–Stokes equations. It is noted that the mathematical expression $p(\mathbf{x},t)+\mathrm{Const}$ can be traced back to the Ladyžhenskaya book [23, p. 47]. It is worthwhile to mention that an arbitrary constant does not depend on spatial variables. To see this, take the gradient operator acting on the pressure scalar field, so we have

$$\begin{aligned}\nabla(p(\mathbf{x},t)+\mathrm{Const}) &= \nabla(p(\mathbf{x},t)) + \underbrace{\nabla(\mathrm{Const})}_{=0}\\ &= \nabla(p(\mathbf{x},t))\end{aligned} \tag{9}$$

In the Ladyžhenskaya review article [24], an arbitrary constant may be dependent on temporal variables. We adopt her notations and define the pressure scalar field such that

$$p(\mathbf{x},t;\mathrm{Const}(t)) = p(\mathbf{x},t)+\mathrm{Const}(t) \tag{10}$$

Equation (10) states that the pressure plus any arbitrary constant varying with time is also a solution of the pressure in the Navier–Stokes system.[‖]

For the incompressible Navier–Stokes equations (cf. Equations (1)–(2)), the dimensionless variables can be constructed by introducing a reference length L and a reference velocity U and given as

$$(x,y)=\frac{1}{L}(x^+,y^+),\quad (u,v)=\frac{1}{U}(u^+,v^+),\quad p=\frac{p^+}{\rho U^2},\quad t=\frac{t^+U}{L},\quad \mathbf{f}=\frac{L}{U^2}\mathbf{f}^+ \tag{11}$$

The symbol $+$ denotes dimensional variables. The variables u^+ and v^+ are the velocity components in x^+ and y^+ directions, p^+ is the pressure, t^+ is the time and $\mathbf{f}^+$ is the force term. Substitution of these variables into Equations (1)–(2) yields

$$\frac{\partial \mathbf{u}}{\partial t}+\mathbf{u}\cdot\nabla\mathbf{u} = -\nabla p+\frac{1}{Re}\nabla^2\mathbf{u}+\mathbf{f} \quad \text{in } \Omega\times(0,T] \tag{12}$$

with

$$\nabla\cdot\mathbf{u}=0 \quad \text{in } \Omega\times[0,T] \tag{13}$$

[‖]If the pressure datum is known beforehand, then the whole pressure scalar field either shifts above the datum by $+\mathrm{Const}(t)\forall t>0$, or below the datum by $-\mathrm{Const}(t)\forall t>0$.

where we have denoted the dimensionless variables by the same symbols as the corresponding dimensional ones. The non-dimensional number $Re = LU/v$ (or inertial force/viscous force), known as the Reynolds number, often serves to characterize the features of the fluid flow field.

3. CONSISTENT SPLITTING SCHEME

Based on the unsteady-state Stokes and hyperbolic systems with the operator-splitting technique, Timmermans *et al.* [25] has investigated the palliations of the artificial Neumann boundary condition for the pressure, in which the correction term for the pressure should be added. By making use of Goda's pressure-correction technique [26], higher-order accuracies for the pressure can be achieved. More significantly, the pressure approximation is no longer spoiled by a numerical boundary layer produced by an artificial Neumann boundary condition (cf. Equation (19)). The mathematical proof of stability analysis on this development was put forward by Guermond and Shen [11]. The latest development of the consistent splitting scheme can be found in Reference [10].

The main ideas of the consistent splitting scheme can be summarized as follows: (1) multiplying Equation (12) by a test function** $\nabla q,\ \forall q \in H^1$ and isolating the pressure gradient as an unknown variable, and then obtaining the weak form of the pressure Poisson equation, (2) using the div-curl identity $\nabla^2\mathbf{u} = \nabla(\nabla\cdot\mathbf{u}) - \nabla\times\nabla\times\mathbf{u} = -\nabla\times\nabla\times\mathbf{u}$ for replacing $\nabla^2\mathbf{u}$, (3) applying Equation (12) for simplifying the non-linear inertial term and source term, and putting the viscous term and time derivative term into the final form, (4) using the gradient operator property for grouping the divergence-free term times the Reynolds number by selecting the arbitrary constant $1/Re$, i.e. $(1/Re)(\nabla^2\mathbf{u} - \nabla\times\nabla\times\mathbf{u}) = (1/Re)\nabla(\nabla\cdot\mathbf{u})$, (5) introducing the auxiliary pressure variable ϕ, and extracting the pressure correction term plus the new term $(1/Re)\nabla\cdot\mathbf{u}$, (6) solving ϕ using Equation (18) first and then the pressure by Equation (19), and (7) keeping the fractional-step projection methods in place, i.e. Equations (17)–(18).

A second-order decoupled approximation to the non-dimensional Navier–Stokes system is defined as follows: Let $\mathbf{u}^0 = \mathbf{u}^{-1} = \mathbf{u}(\mathbf{x}, 0),\ p^0 = p^{-1} = p(\mathbf{x}, 0)$. Let $(\mathbf{u}^n, p^n)$ be the nth time-step to $(\mathbf{u}(\mathbf{x}, n\Delta t), p(\mathbf{x}, n\Delta t))$. For $n = 1$, find $\mathbf{u}^1$ and p^1 such that

$$\begin{gathered}\frac{\mathbf{u}^1 - \mathbf{u}^0}{\Delta t} + (\mathbf{u}^0\cdot\nabla)\mathbf{u}^1 + \frac{1}{2}(\nabla\cdot\mathbf{u}^0)\mathbf{u}^1 - \frac{1}{Re}\nabla^2\mathbf{u}^1 + \nabla p^0 = \mathbf{f}^1 \\ \mathbf{u}^1|_{\partial\Omega} = \mathbf{b}^1\end{gathered} \tag{14}$$

**On Ω, the space of square integrable functions

$$L^2(\Omega) := \left\{ q \,\middle|\, \int_\Omega |q|^2 \,\mathrm{d}\Omega < \infty \right\}$$

and the subspace

$$H^1(\Omega) := \{ w | w \in L^2(\Omega), \operatorname{grad} w \in (L^2(\Omega))^{nd} \}$$

of $L^2(\Omega)$ are defined, where nd is the space dimension of the problem.

$$(\nabla\phi^1, \nabla q) = \left(\frac{\mathbf{u}^1 - \mathbf{u}^0}{\Delta t}, \nabla q\right) \quad \forall q \in H^1(\Omega) \tag{15}$$

$$p^1 = \phi^1 + p^0 - \frac{1}{Re}\nabla \cdot \mathbf{u}^1 \tag{16}$$

Note that we use the first-order discretization in space, together with the backward Euler discretization in time. Then, for $n \geqslant 1$, find $\mathbf{u}^{n+1}$ and p^{n+1} such that

$$\begin{aligned} &\frac{3\mathbf{u}^{n+1} - 4\mathbf{u}^n + \mathbf{u}^{n-1}}{2\Delta t} + ((2\mathbf{u}^n - \mathbf{u}^{n-1}) \cdot \nabla)\mathbf{u}^{n+1} + \frac{1}{2}(\nabla \cdot (2\mathbf{u}^n - \mathbf{u}^{n-1}))\mathbf{u}^{n+1} \\ &\quad - \frac{1}{Re}\nabla^2\mathbf{u}^{n+1} + \nabla(2p^n - p^{n-1}) = \mathbf{f}^{n+1} \\ &\mathbf{u}^{n+1}|_{\partial\Omega} = \mathbf{b}^{n+1} \end{aligned} \tag{17}$$

$$(\nabla\phi^{n+1}, \nabla q) = \left(\frac{3\mathbf{u}^{n+1} - 4\mathbf{u}^n + \mathbf{u}^{n-1}}{2\Delta t}, \nabla q\right) \quad \forall q \in H^1(\Omega) \tag{18}$$

$$p^{n+1} = \phi^{n+1} + 2p^n - p^{n-1} - \frac{1}{Re}\nabla \cdot \mathbf{u}^{n+1} \tag{19}$$

The boundary conditions on the velocity $\mathbf{u}^{n+1}|_{\partial\Omega} = \mathbf{b}^{n+1}$ are essential.

3.1. Temporal discretization

A fully implicit second-order backward differentiation formula (BDF) is used for the time derivative that is of accuracy $\mathcal{O}(\Delta t^2)$, i.e.

$$\left(\frac{\partial \mathbf{u}}{\partial t}\right)^{n+1} = \frac{3\mathbf{u}^{n+1} - 4\mathbf{u}^n + \mathbf{u}^{n-1}}{2\Delta t} + \mathcal{O}(\Delta t^2) \tag{20}$$

This scheme is usually recommended for the time discretization of the time derivative term, because the scheme is stable and second-order accurate.

3.2. Treatment of non-linear term

The treatment of the non-linear advection term transformed into a linear advection one using a linear extrapolation in time was discussed by Turek [27]. The non-linear term $(\mathbf{u}^{n+1} \cdot \nabla)\mathbf{u}^{n+1}$ is replaced in a semi-implicit way by $(\mathbf{u}^n \cdot \nabla)\mathbf{u}^{n+1}$ or $((2\mathbf{u}^n - \mathbf{u}^{n-1}) \cdot \nabla)\mathbf{u}^{n+1}$. The two corresponding terms have different numerical accuracies in each time step. The former is of first-order only, while the latter is of second order. As suggested by Témam [3, 4] and considered by many others (see e.g. Reference [28, p. 444]), adding the kinetic term that is regarded somewhat as the skew-symmetric form can have no restriction on the choice of time step Δt, which guarantees an unconditional stability. To enhance the accuracy, we use $\frac{1}{2}(\nabla \cdot (2\mathbf{u}^n - \mathbf{u}^{n-1}))\mathbf{u}^{n+1}$. More importantly, when the approximate velocity fields do not exactly satisfy the incompressibility condition, this term plays an essential rôle in preserving the dissipativity of the discrete system (see e.g. Reference [29]).

3.3. Homogenous Neumann boundary condition

When working on the homogenous Neumann boundary condition, one has to pay special attention; it is well known that the solution of Equation (18) is known up to an additional constant when subjected to the homogenous Neumann boundary condition [30, Chapter xi]. As noted in literature, there are two common ways of obtaining a pressure scalar field solution uniquely to the NS system. It can be done by

Option I: Imposing an additional condition on $\phi(\mathbf{x}, t; \text{Const}(t))$ such as specifying one point $\phi(x_0, y_0, t; \text{Const}(t))$ on the boundary $\partial\Omega$ (a point of interest (x_0, y_0) must be adjusted)
Option II: Requiring that the integral of $\phi(\mathbf{x}, t; \text{Const}(t))$ over Ω is equal to zero or can be interpreted as the average value, i.e.

$$\int_\Omega \phi(\mathbf{x}, t; \text{Const}(t))\, \mathrm{d}\Omega = 0 \tag{21}$$

In the course of the numerical calculation for solving a singular (elliptic) Poisson problem, one may run into these two options. For the study of the first option in hydrodynamic stability, see e.g. Reference [23, Chapter 1, p. 24] and especially the surveys [31, p. 55; 32, p. 152]. To remedy this difficulty more handily, a fixed Dirichlet pressure boundary value on the boundary that does not vary with time is commonly found in applications of flow physics problems such as the 2D lid-driven cavity (see e.g. Reference [33, p. 33] or [34, p. 121]). Assigning a fixed value is also directly suited for the numerical verification of some existing numerical schemes [25]. This will be the measure that we shall use for our numerical calculations in this paper.

3.4. Spatial discretization

The finite element formulations based on the Galerkin weighted residual approach are used for the discretization of the governing equations. Velocities, auxiliary pressures and pressures are taken as the primitive unknown variables. By first multiplying Equations (17)–(19) by corresponding test functions $\mathbf{w}$, q, and m, and integrating the corresponding equations over Ω, using the integration by parts in Equation (17), and choosing $\mathbf{w}$ with a zero trace on $\partial\Omega$, find $(\mathbf{u}, \phi, p) \in \mathbf{X} \times H^1(\Omega) \times L^2(\Omega)$ such that

$$\begin{aligned}
&\forall \mathbf{w} \in \mathbf{X}_0 = (H_0^1(\Omega))^2 \quad \text{with } \mathbf{w}|_{\partial\Omega} = 0: \\
&\left(\frac{3\mathbf{u}^{n+1} - 4\mathbf{u}^n + \mathbf{u}^{n-1}}{2\Delta t}, \mathbf{w}\right) \\
&\quad + \left(((2\mathbf{u}^n - \mathbf{u}^{n-1}) \cdot \nabla)\mathbf{u}^{n+1} + \frac{1}{2}(\nabla \cdot (2\mathbf{u}^n - \mathbf{u}^{n-1}))\mathbf{u}^{n+1}, \mathbf{w}\right) \\
&\quad + \frac{1}{Re}(\nabla \mathbf{u}^{n+1}, \nabla \mathbf{w}) - (2p^n - p^{n-1}, \nabla \cdot \mathbf{w}) = (\mathbf{f}^{n+1}, \mathbf{w}) \\
&\mathbf{u}^{n+1}|_{\partial\Omega} = \mathbf{b}^{n+1} \\
&\qquad \forall q \in H^1(\Omega):
\end{aligned} \tag{22}$$

$$(\nabla\phi^{n+1}, \nabla q) = \left(\frac{3\mathbf{u}^{n+1} - 4\mathbf{u}^n + \mathbf{u}^{n-1}}{2\Delta t}, \nabla q\right) \tag{23}$$

$\forall m \in L^2(\Omega)$:

$$(p^{n+1}, m) = \left(\phi^{n+1} + 2p^n - p^{n-1} - \frac{1}{Re}\nabla\cdot\mathbf{u}^{n+1}, m\right) \tag{24}$$

The finite element approximation of the given problem is obtained simply by replacing the functional space $\mathbf{X}\times H^1(\Omega)\times L^2(\Omega)$ in Equations (22)–(24) by the finite element subspace $\mathbf{X}_h\times Q_h\times M_h$ such that: Find $(\mathbf{u}_h, \phi_h, p_h)\in\mathbf{X}_h\times Q_h\times M_h$ such that

$$\begin{aligned}
&\forall \mathbf{w}_h \in \mathbf{X}_{0,h} \quad \text{with } \mathbf{w}_h|_{\partial\Omega} = 0:\\
&\left(\frac{3\mathbf{u}_h^{n+1} - 4\mathbf{u}_h^n + \mathbf{u}_h^{n-1}}{2\Delta t}, \mathbf{w}_h\right)\\
&\quad + \left(((2\mathbf{u}_h^n - \mathbf{u}_h^{n-1})\cdot\nabla)\mathbf{u}_h^{n+1} + \frac{1}{2}(\nabla\cdot(2\mathbf{u}_h^n - \mathbf{u}_h^{n-1}))\mathbf{u}_h^{n+1}, \mathbf{w}_h\right)\\
&\quad + \frac{1}{Re}(\nabla\mathbf{u}_h^{n+1}, \nabla\mathbf{w}_h) - (2p_h^n - p_h^{n-1}, \nabla\cdot\mathbf{w}_h) = (\mathbf{f}^{n+1}, \mathbf{w}_h)\\
&\mathbf{u}_h^{n+1}|_{\partial\Omega} = \mathbf{b}^{n+1}
\end{aligned} \tag{25}$$

$\forall q_h \in Q_h$:

$$(\nabla\phi_h^{n+1}, \nabla q_h) = \left(\frac{3\mathbf{u}_h^{n+1} - 4\mathbf{u}_h^n + \mathbf{u}_h^{n-1}}{2\Delta t}, \nabla q_h\right) \tag{26}$$

$\forall m_h \in M_h$:

$$(p_h^{n+1}, m_h) = \left(\phi_h^{n+1} + 2p_h^n - p_h^{n-1} - \frac{1}{Re}\nabla\cdot\mathbf{u}_h^{n+1}, m_h\right) \tag{27}$$

The mixed finite element of choice is the Taylor-Hood type, and $\{\mathbb{P}_2, \mathbb{P}_1, \mathbb{P}_1\}$ elements and their respective shape functions are used, as illustrated in Figure 2. This choice verifies the discrete inf–sup condition, which ensures the uniqueness and existence of the solution of the discrete version of the steady Stokes problem. For a complete discussion, we refer the reader to References [35, 36]. Let us introduce a regular triangulation of Ω, with a finite number of triangles K_l, $l = 1, N_h$, where N_h stands for the total number of triangles. We define X_h by

$$X_h = \{w_h \in C^0(\Omega) : w_h|_{K_l} \in \mathbb{P}_2, \forall l = 1, N_h\} \tag{28}$$

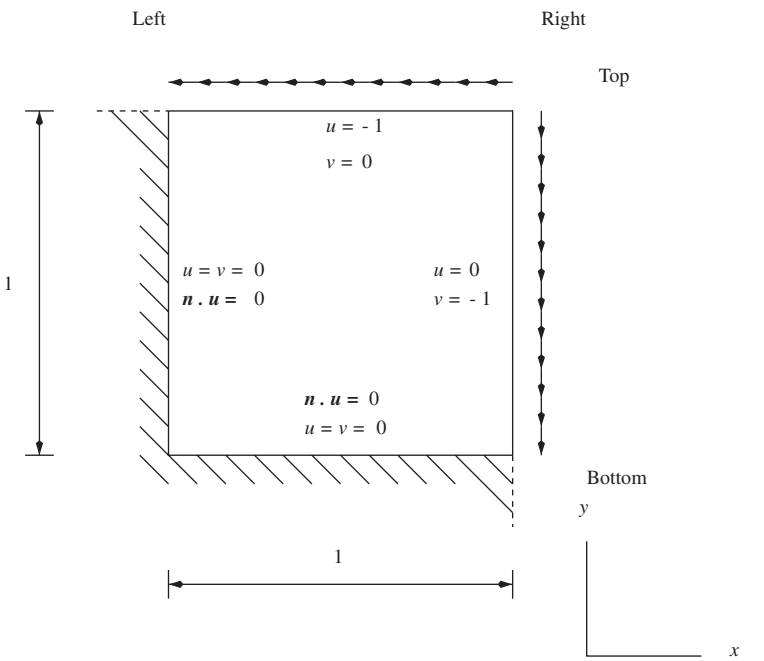

Figure 1. Geometry of the 2D double lid-driven cavity with velocity boundary conditions.

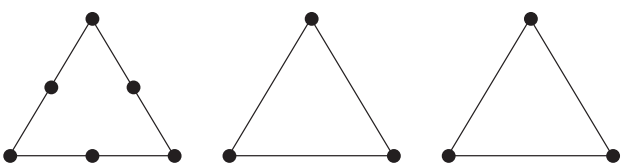

Figure 2. $\{\mathbb{P}_2, \mathbb{P}_1, \mathbb{P}_1\}$ for $\{\mathbf{u}_h, \phi_h, p_h\}$.

and then define Q_h by

$$Q_h = \{q_h \in C^0(\Omega) : q_h|_{K_l} \in \mathbb{P}_1, \forall l = 1, N_h\} \tag{29}$$

and finally define M_h by

$$M_h = \{m_h \in C^0(\Omega) : m_h|_{K_l} \in \mathbb{P}_1, \forall l = 1, N_h\} \tag{30}$$

the space $\mathbb{P}_r$ denote the sets of polynomials of degree r in each K_l, i.e. for $r \geqslant 0$:

$$\mathbb{P}_r := \left\{ w : K_l \to \mathbb{R}, w(x, y) = \sum_{0 \leqslant i+j \leqslant r} \alpha_{ij} x^i y^j \right\} \tag{31}$$

After the domain is discretized into finite elements, local element matrices are first calculated, and then assembled to form global matrices. The matrix forms of Equations (25)–(27) are

(1) Given approximate velocities, $\{U_h^n, U_h^{n-1}, V_h^n, V_h^{n-1}\}$, and corresponding pressures $\{P_h^n, P_h^{n-1}\}$, solve

$$\left[\frac{3}{2\Delta t}\mathsf{M} + \mathsf{C}_{2U_h^n - U_h^{n-1}} + \mathsf{C}_{2V_h^n - V_h^{n-1}} + \frac{1}{2}\mathsf{K}_{[2U_h^n - U_h^{n-1}, 2V_h^n - V_h^{n-1}]} + \frac{1}{Re}\mathsf{S}\right] U_h^{n+1}$$

$$= \frac{2}{\Delta t}\mathsf{M}U_h^n - \frac{1}{2\Delta t}\mathsf{M}U_h^{n-1} + \mathsf{F}_U^{n+1} - \mathsf{DX}(2P_h^n - P_h^{n-1}) \tag{32}$$

and

$$\left[\frac{3}{2\Delta t}\mathsf{M} + \mathsf{C}_{2U_h^n - U_h^{n-1}} + \mathsf{C}_{2V_h^n - V_h^{n-1}} + \frac{1}{2}\mathsf{K}_{[2U_h^n - U_h^{n-1}, 2V_h^n - V_h^{n-1}]} + \frac{1}{Re}\mathsf{S}\right] V_h^{n+1}$$

$$= \frac{2}{\Delta t}\mathsf{M}V_h^n - \frac{1}{2\Delta t}\mathsf{M}V_h^{n-1} + \mathsf{F}_V^{n+1} - \mathsf{DY}(2P_h^n - P_h^{n-1}) \tag{33}$$

for approximate velocities at time t^{n+1}.

(2) Using approximate velocities, solve the auxiliary pressure Φ_h^{n+1}

$$\hat{\mathsf{S}}\Phi_h^{n+1} = -\frac{1}{\Delta t}\left(\widehat{\mathsf{DX}}\left(\frac{3U_h^{n+1} - 4U_h^n + U_h^{n-1}}{2}\right) + \widehat{\mathsf{DY}}\left(\frac{3V_h^{n+1} - 4V_h^n + V_h^{n-1}}{2}\right)\right) \tag{34}$$

(3) Using approximate velocities, solve the transfer pressure Π_h^{n+1}

$$\hat{\mathsf{M}}\Pi_h^{n+1} = -\frac{1}{Re}(\widehat{\mathsf{DX}}U_h^{n+1} + \widehat{\mathsf{DY}}V_h^{n+1}) \tag{35}$$

(4) Update the pressure at time t^{n+1} viz.

$$P_h^{n+1} = \Pi_h^{n+1} + (\Phi_h^{n+1} + 2P_h^n - P_h^{n-1}) \tag{36}$$

(5) Repeat steps 1–4 until a final number of time steps is reached.

For the sake of clarity, U_h^{n+1}, V_h^{n+1}, Φ_h^{n+1}, Π_h^{n+1} and P_h^{n+1} are the vectors containing unknowns at the $(n+1)$th time step and M, $\mathsf{C}_{2U_h^n - U_h^{n-1}}$, $\mathsf{C}_{2V_h^n - V_h^{n-1}}$, $\mathsf{K}_{[2U_h^n - U_h^{n-1}, 2V_h^n - V_h^{n-1}]}$, S, DX, DY, F_U^{n+1} and F_V^{n+1} represent the consistent mass matrix, the convective matrix w.r.t[††] the u-comp.,[‡‡] the convective matrix w.r.t the v-comp., the kinetic matrix, the diffusion matrix, the gradient matrix w.r.t the x-comp., the gradient matrix w.r.t the y-comp., the force vector w.r.t the x-comp., and the force vector w.r.t the y-comp, respectively, and $\hat{\mathsf{S}}$, $\widehat{\mathsf{DX}}$, $\widehat{\mathsf{DY}}$ and $\hat{\mathsf{M}}$ denote the diffusion

[††] with respect to
[‡‡] component

matrix, the divergence matrix w.r.t the x-comp., the divergence matrix w.r.t the y-comp. and the consistent mass matrix, respectively.

Remarks

The following numerical implementations were made within an in-house code that was based on the above algorithm.

(i) To compute all the element integrals we use classical quadrature formulae of Gaussian type. The integration over the triangles is performed in terms of the Gaussian quadrature rules using a four-point formula for the $\mathbb{P}_1$ interpolation and a seven-point formula for the $\mathbb{P}_2$ interpolation.

(ii) Except the convective and kinetic matrices, all the matrices are computed once and stored in sparse matrix formats.

(iii) Operated with the SPARSKIT package borrowed from Saad [37], preconditioners for sparse GMRES iterative solvers derived from threshold-based ILUT factorizations were used. The following selective parameters were used for all performance tests unless otherwise stated: the number of fill-in elements per row is 50; calculation is terminated when the relative precision is below $\varepsilon = 10^{-8}$; and convergence of the iterative process was fixed by a specific number of iteration. We shall provide more details in Section 4.

(iv) Let $N_{\mathrm{v}} = \dim(X_h)$ and $N_p = \dim(M_h)$ (or $N_\phi = \dim(Q_h)$) be the total number of velocity/pressure (or auxiliary pressure) interpolation nodes in term of the mixed FE approximation (i.e. $\mathbb{P}_2/\mathbb{P}_1$). To assign the dimensionality of two different types of matrices, $\{\mathsf{DX}, \mathsf{DY}\}$ and $\{\widehat{\mathsf{DX}}, \widehat{\mathsf{DY}}\}$, we have $N_{\mathrm{v}} \times N_p$ and $N_p \times N_{\mathrm{v}}$, respectively. To link between two different types of FE interpolations and match the same degree of freedom of $\{P_h^n, P_h^{n-1}\}$ in step 1, $\{U_h^{n+1}, U_h^n, U_h^{n-1}\}$ in step 2 and $\{V_h^{n+1}, V_h^n, V_h^{n-1}\}$ in step 2, all these coefficient matrices are of rectangular form. The integration over the triangles is performed in terms of the Gaussian quadrature rules using a seven-point formula for a combination of $\mathbb{P}_1$ and $\mathbb{P}_2$. Another way to calculate the gradient matrices that maintain a full rank is by the $\mathbb{P}_2$ FE approximation. In doing so, we take the average value between two functional values in step 4 in order to match the same degree of freedom of $\{P_h^n, P_h^{n-1}\}$ in step 1.

(v) A unique solution to the matrix system (cf. Equation (34)) will be obtained

(a) either by imposing condition Φ_h^{n+1} such as specifying ϕ_0 at one point on the boundary $\partial\Omega$ and by assigning *a priori* known value in Φ_h^{n+1}

$$\begin{bmatrix} 1 & 0 & \cdots & 0 \\ * & * & \cdots & \cdots \\ \vdots & \vdots & \ddots & * \\ * & \vdots & * & \ddots \end{bmatrix} \begin{Bmatrix} \phi_1 \\ \vdots \\ \vdots \\ \vdots \end{Bmatrix} = \begin{Bmatrix} \phi_0 \\ \vdots \\ \vdots \\ \vdots \end{Bmatrix} \tag{37}$$

Let us consider the first row of the matrix $\hat{\mathsf{S}}$. Assign a unity value in the first position and zero values for the other positions. Then the rank of the matrix $\hat{\mathsf{S}}$ is

lowered by one by deleting one equation, i.e. there is no need for determining the value ϕ_1. After this procedure, the matrix $\hat{\mathsf{S}}$ safely becomes non-singular.

(b) or by solving the augmented system [38, p. 115] such that

$$\begin{bmatrix} \hat{\mathsf{S}} & r \\ r^{\hat{t}} & 0 \end{bmatrix} \begin{Bmatrix} \Phi_h^{n+1} \\ \phi \end{Bmatrix} = \begin{Bmatrix} \mathsf{G}^{n+1} \\ 0 \end{Bmatrix} \tag{38}$$

where $r = \{1, \ldots, 1\}$ is the right null vector of $\hat{\mathsf{S}}$, $\hat{t}$ denotes the transpose of r and G^{n+1} denotes the right-hand side of Equation (34). The last equation will set the mean value of ϕ to zero.

4. NUMERICAL RESULTS FOR THE NAVIER–STOKES PROBLEM

For the study of the temporal convergence of the BDF splitting error with the Reynolds number, we choose the following test flow problem that was used by Pearson [39], Chorin [1], Braza *et al.* [40], Mansutti *et al.* [41], Strikwerda [42] and others to examine their methods. This flow was initialized by Taylor [43] in 1923 for the physical case of a system of vortices built in a square pattern. It emerges in a cellular flow, consisting of eddies which rotate alternative in opposite directions and whose intensity is decayed over time by the effect of viscosity [41]. As quoted by many researchers, the most classical 2D worked example, that belongs to a special sub-branch of the Beltrami flows [44] is summarized as

$$u(x, y, t) = -\cos(x)\sin(y)\mathrm{e}^{-2t/Re} \tag{39}$$

$$v(x, y, t) = \sin(x)\cos(y)\mathrm{e}^{-2t/Re} \tag{40}$$

$$p(x, y, t) = -\tfrac{1}{4}(\cos(2x) + \cos(2y))\mathrm{e}^{-4t/Re} \tag{41}$$

We want to show a numerical result. Assuming that $Re = 1$ we solve Equations (17)–(19) for $\Omega = [-\pi, \pi] \times [-\pi, \pi]$. Equations (39)–(40) satisfy the incompressibility constraint. For the case of $Re = 1$, the solution dies off rapidly against Δt which is good for testing the efficiency of time integration. The time t runs from $[0, 1]$ with varying time step Δt. We accomplished these assumptions by imposing the analytical solutions on the initial velocity fields, on the pressure and at the boundary $\partial\Omega$.

In order to uncover more hidden information both from the velocity and pressure boundary layers and from the corner vortices, it is useful to produce a thin layer within the domain, which not only maintains the uniform mesh structure but also has a concentration of triangles along the boundaries. This so-called boundary-refined mesh was used in the Gervais *et al.* paper [45] for studying a stability analysis of the 2D lid-driven cavity. The boundary-refined mesh is defined as the conformal image of the uniform mesh on $[0, 1]^2$ by the 2D mapping:

$$X(i) = \sin^2\left(\frac{\pi}{2}x(i)\right), \quad Y(i) = \sin^2\left(\frac{\pi}{2}y(i)\right) \tag{42}$$

where i denotes the number of nodes, and $x(i)$, $y(i)$ are sets of 2D uniform mesh cöordinates, and $X(i)$, $Y(i)$ are sets of 2D boundary-refined mesh cöordinates. The finer the mesh refinement, the thinner the layers. For the illustrative purposes, the 2D boundary-refined meshes are

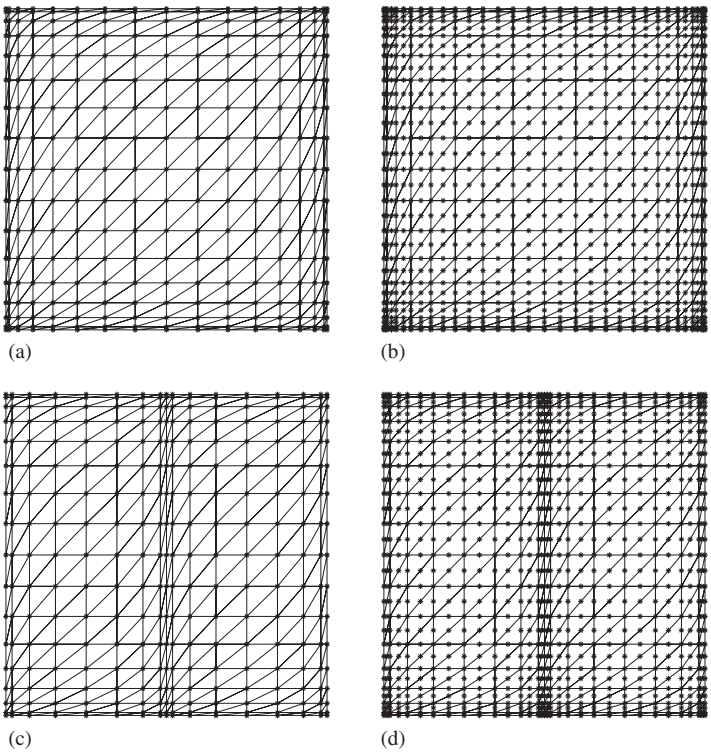

Figure 3. Panels (a) and (b) are 2D boundary-refined meshes in two FE ($\mathbb{P}_1/\mathbb{P}_2$) spaces. Panels (c) and (d) are 2D 2-cell boundary-refined meshes in two FE ($\mathbb{P}_1/\mathbb{P}_2$) spaces.

Table I. Detail on convergence of the iterative process; $G_1 : 129 \times 129/65 \times 65$, $G_2 : 257 \times 257/129 \times 129$, $G_3 : 513 \times 513/257 \times 257$.

	G_1	G_2	G_3
u (cf. Equation (32))	10	9	14
v (cf. Equation (33))	10	9	14
ϕ (cf. Equation (34))	10	14	22
p (cf. Equation (35))	4	4	4
ω (cf. Equation (43))	4	4	4
ψ (cf. Equation (45))	10	17	29

depicted in Figure 3. To verify the convergence rate with respect to the spatial discretization, we select the grid range from 65×65 to 513×513. Table I shows the convergence of the iterative process that was obtained in the optimal number of iterations.

Through a series of numerical experiments we obtained the rate of convergence for $Re = 1$. Figures show the error norms against the time step size for different choices of the mesh size. Scales on both axes are logarithmic. The slopes of the lines allow an estimate of the rate of

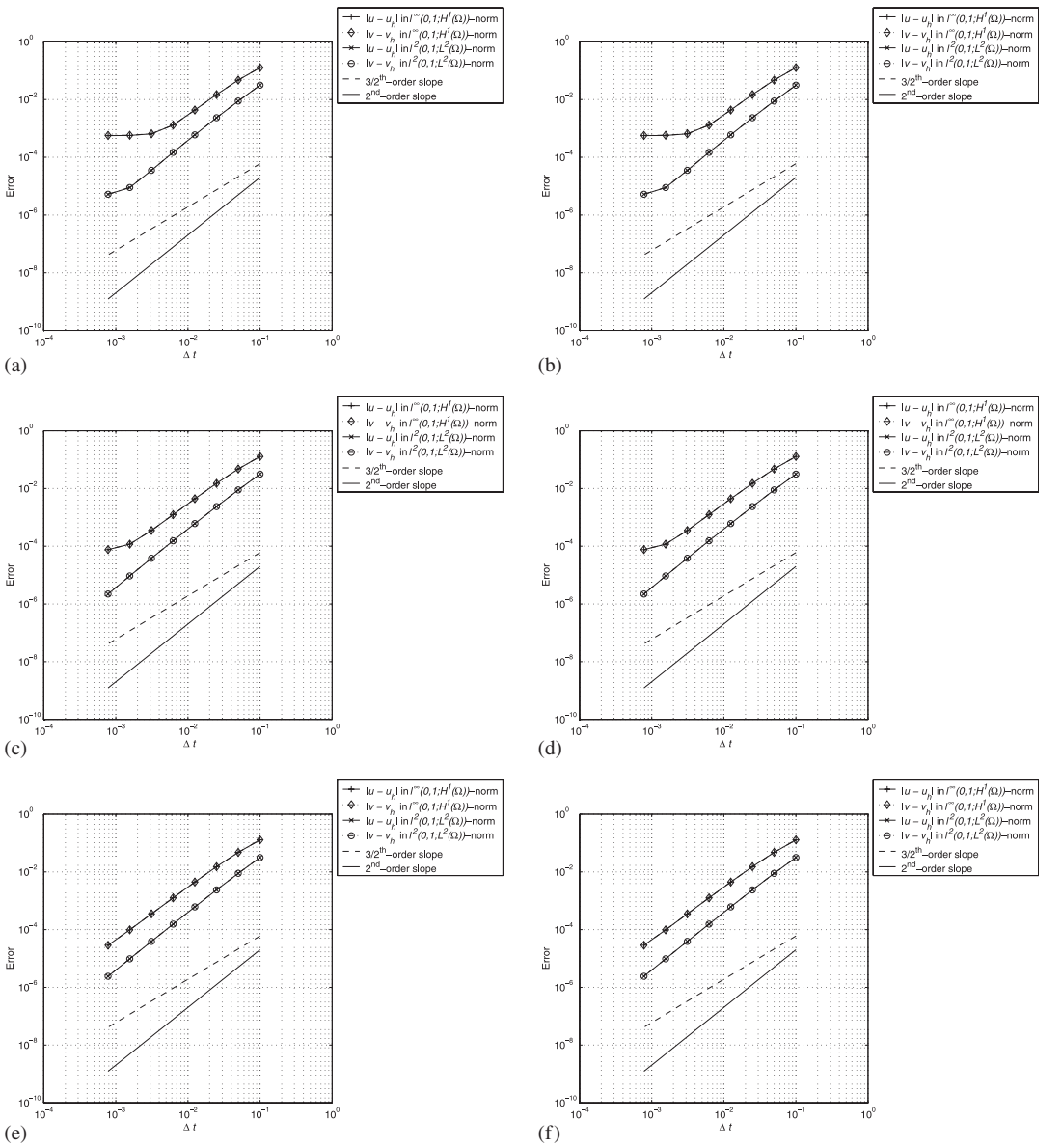

Figure 4. Convergence results for the velocity fields at $Re = 1$ and $T = 1$ using a pressure point boundary value in the left panel and using the augmented system in the right panel: (a) and (b) 129×129 grid; (c) and (d) 257×257 grid; and (e) and (f) 513×513 grid.

convergence. Until stated otherwise, the $\mathbb{P}_2$ gradient matrix formulation in concert with the average procedure of the linear pressure nodes in step 1 is used for all the numerical simulations.

In Figures 4 and 5 the observed rates of convergence are compared with the expected rates. As for the $|\cdot|_{l^\infty(0,T;H^1(\Omega))}$- and $\|\cdot\|_{l^2(0,T;L^2(\Omega))}$-errors of the approximate velocity fields, the

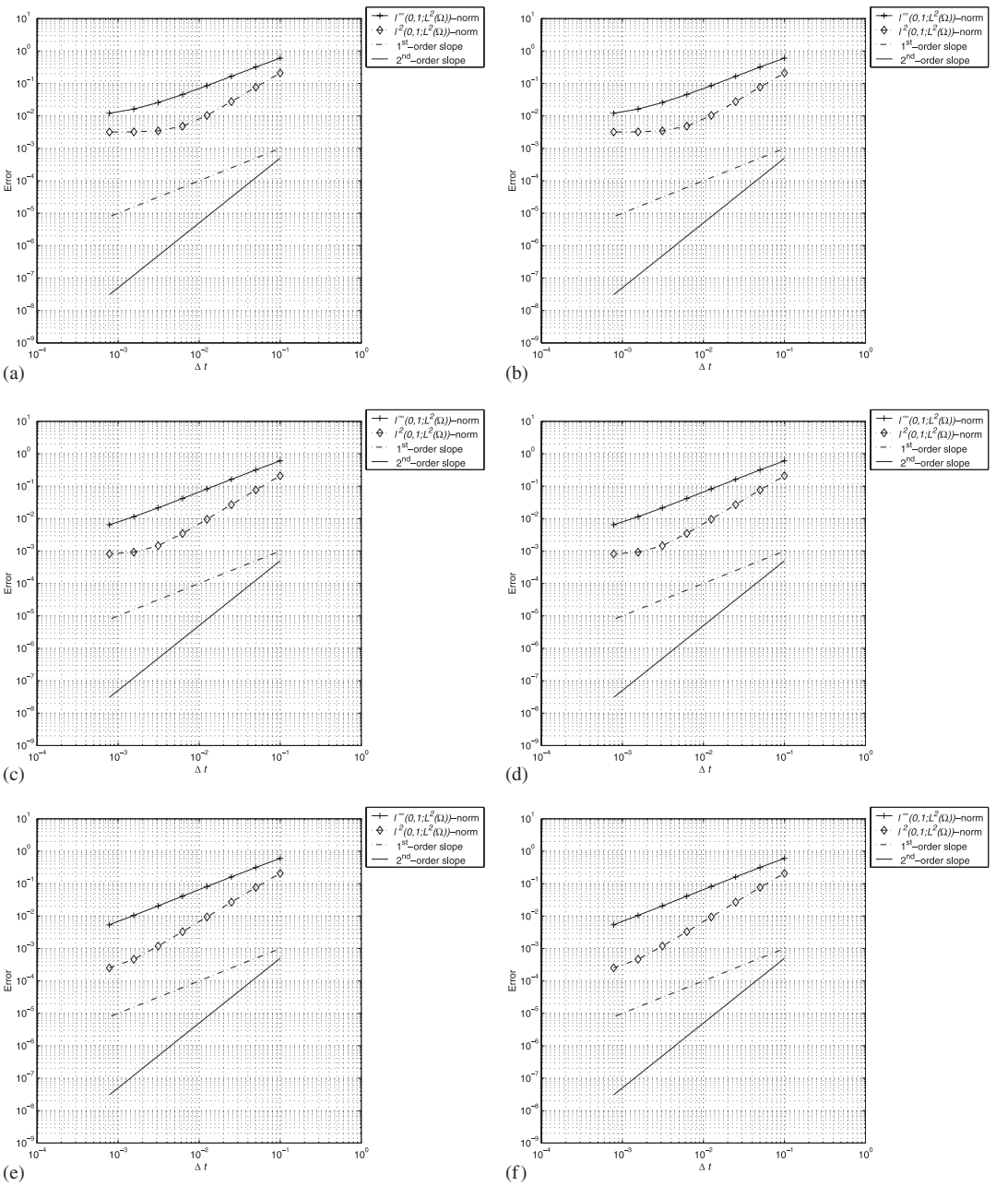

Figure 5. Convergence results for the pressure at $Re = 1$ and $T = 1$ using a pressure point boundary value in the left panel and using the augmented system in the right panel: (a) and (b) 65×65 grid; (c) and (d) 129×129 grid; and (e) and (f) 257×257 grid.

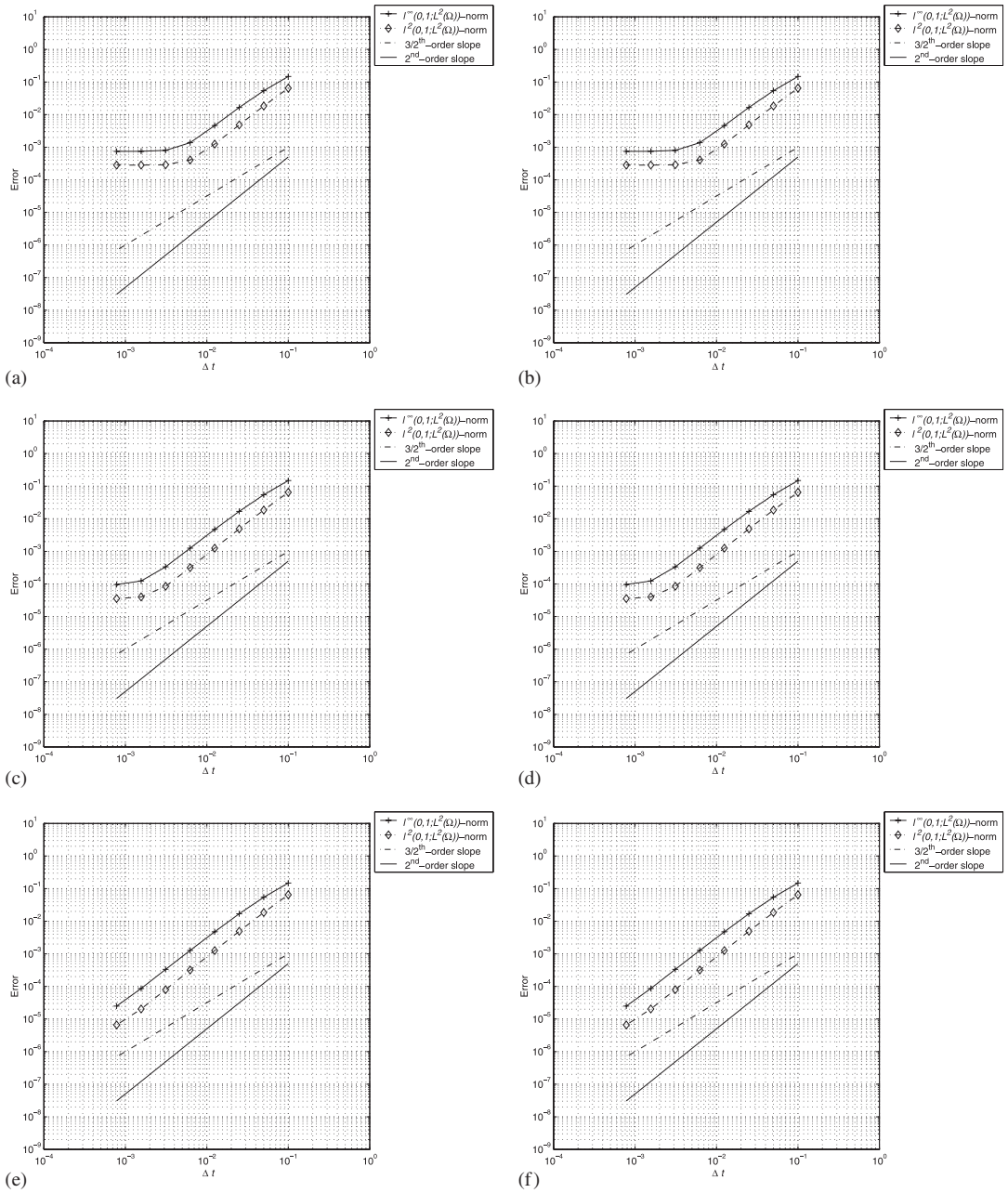

Figure 6. Convergence results for the divergence-free velocity fields at $Re = 1$ and $T = 1$ using a pressure point boundary value in the left panel and using the augmented system in the right panel: (a) and (b) 129×129 grid; (c) and (d) 257×257 grid; and (e) and (f) 513×513 grid.

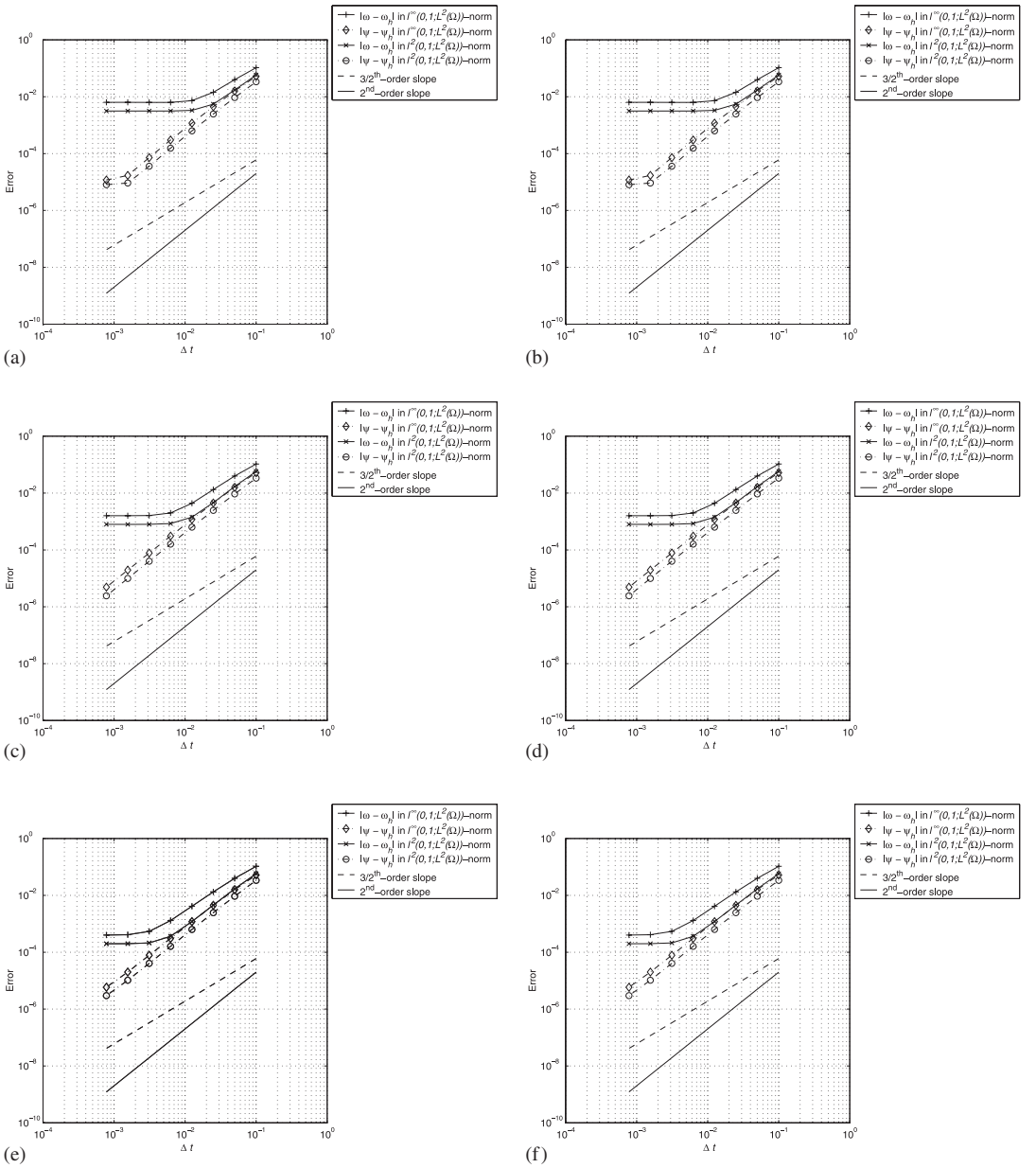

Figure 7. Convergence results for the vorticity/stream-function at $Re = 1$ and $T = 1$ using a pressure point boundary value in the left panel and using the augmented system in the right panel: (a) and (b) 129×129 grid; (c) and (d) 257×257 grid; and (e) and (f) 513×513 grid.

scheme appears to have the expected convergence rates of $\mathcal{O}(\Delta t^2)$. As for the $\|\cdot\|_{l^\infty(0,T;L^2(\Omega))}$ and $\|\cdot\|_{l^2(0,T;L^2(\Omega))}$-errors of the approximate pressure, one infers from the figures that convergence rates are in $\mathcal{O}(\Delta t)$ and $\mathcal{O}(\Delta t^2)$, respectively. As the reader can note, the rate of

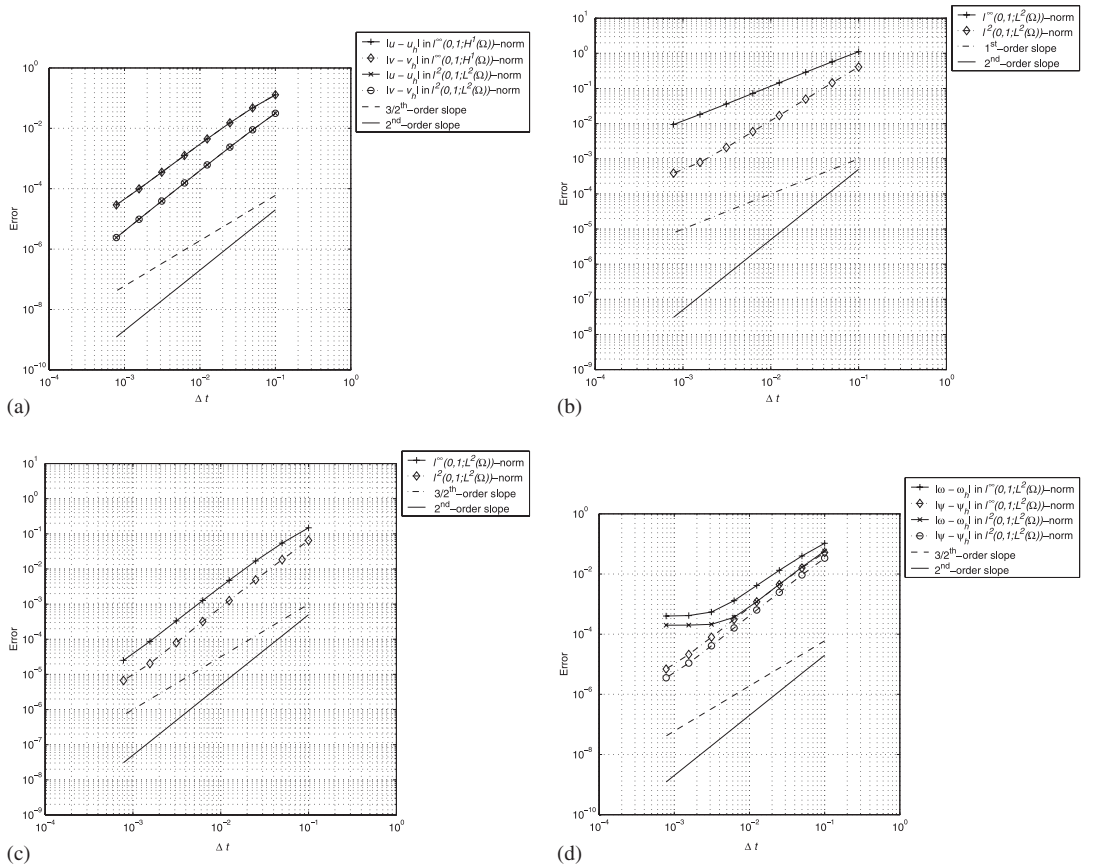

Figure 8. Convergence results for the velocity, pressure, divergence-free and vorticity/stream-function at $Re = 1$ and $T = 1$ using the augmented system: (a) velocity: 513×513 grid; (b) pressure: 257×257 grid; (c) divergence-free: 513×513 grid; and (d) vorticity/stream-function: 513×513 grid.

convergence for the pressure does not exhibit a quadratic decay in time. As suggested, when the grid size is not fine enough, a reduction of the parameter Δt does not enhance the accuracy.

The error $l^\infty(0, T; L^2(\Omega))$ and $l^2(0, T; L^2(\Omega))$-norm calculations with respect to the FE mesh refinement of spatial grids and the temporal refinement of time-steps are presented in Figure 6. In all cases the convergent rate of approximate divergence-free velocities is of $\mathcal{O}(h^2 + \Delta t^2)$.

A vorticity ω is defined by

$$\omega = \frac{\partial v}{\partial x} - \frac{\partial u}{\partial y} \tag{43}$$

We define a stream-function ψ such that

$$u = \frac{\partial \psi}{\partial y} \quad \text{and} \quad v = -\frac{\partial \psi}{\partial x} \tag{44}$$

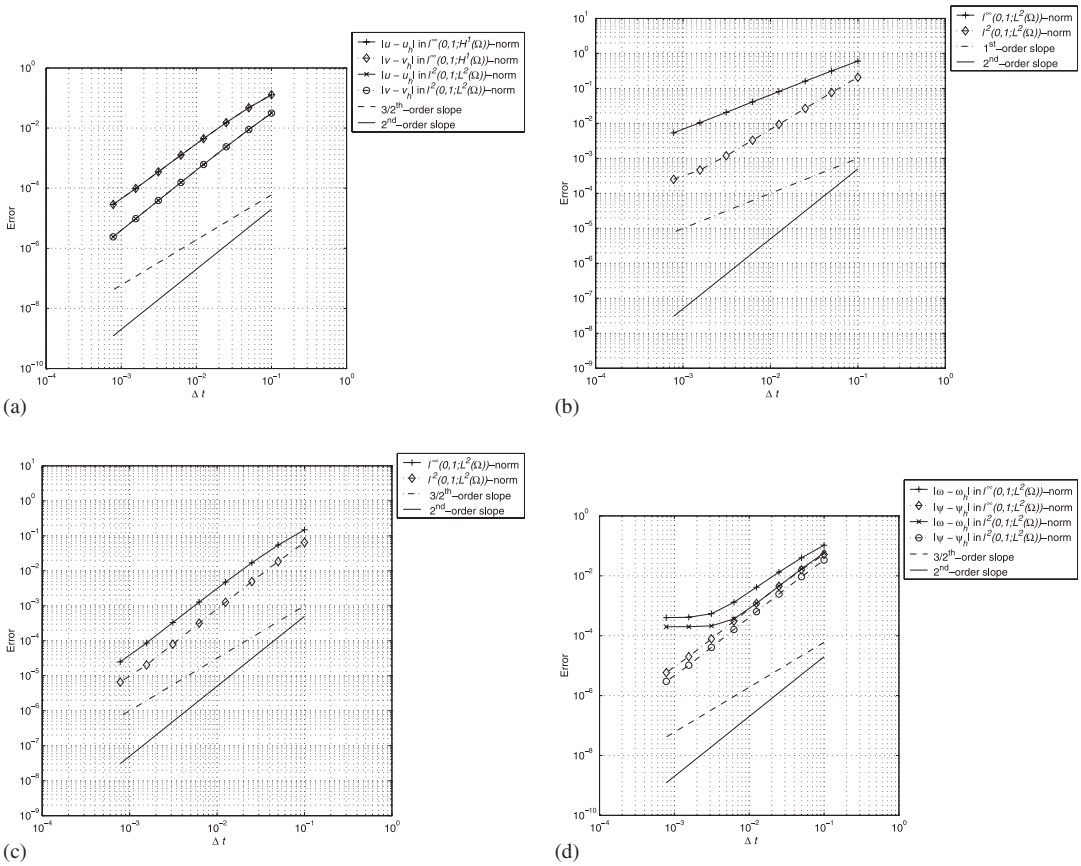

Figure 9. Convergence results for the velocity, pressure, divergence-free and vorticity/stream-function at $Re = 1$ and $T = 1$ using the augmented system and the rectangular gradient matrix approximation: (a) velocity: 513×513 grid; (b) pressure: 257×257 grid; (c) divergence-free: 513×513 grid; and (d) vorticity/stream-function: 513×513 grid.

From Equations (43) and (44), it follows from that

$$\nabla^2 \psi = -\omega \tag{45}$$

In the FE literature, it is customary to calculate the vorticity ω using the consistent mass matrix problem and the stream-function ψ using the Dirichlet problem. The Dirichlet boundary condition for the stream-function is considered. In Figure 7, we display the errors as a function of time. In all vorticity/stream-function variables the convergence rate of the $l^\infty(0,T;L^2(\Omega))$- and $l^2(0,T;L^2(\Omega))$-norm estimations is second-order accurate in time.

Figures 3(c) and (d) show the mixed finite element mesh for the third problem (cf. Section 5.3). The mesh is refined near all the walls and along the middle of the cavity. In Figure 8, we show the errors as a function of time using the two-cell boundary-refined mesh layout. We restrict ourselves to using the augmented system for calculating the auxiliary

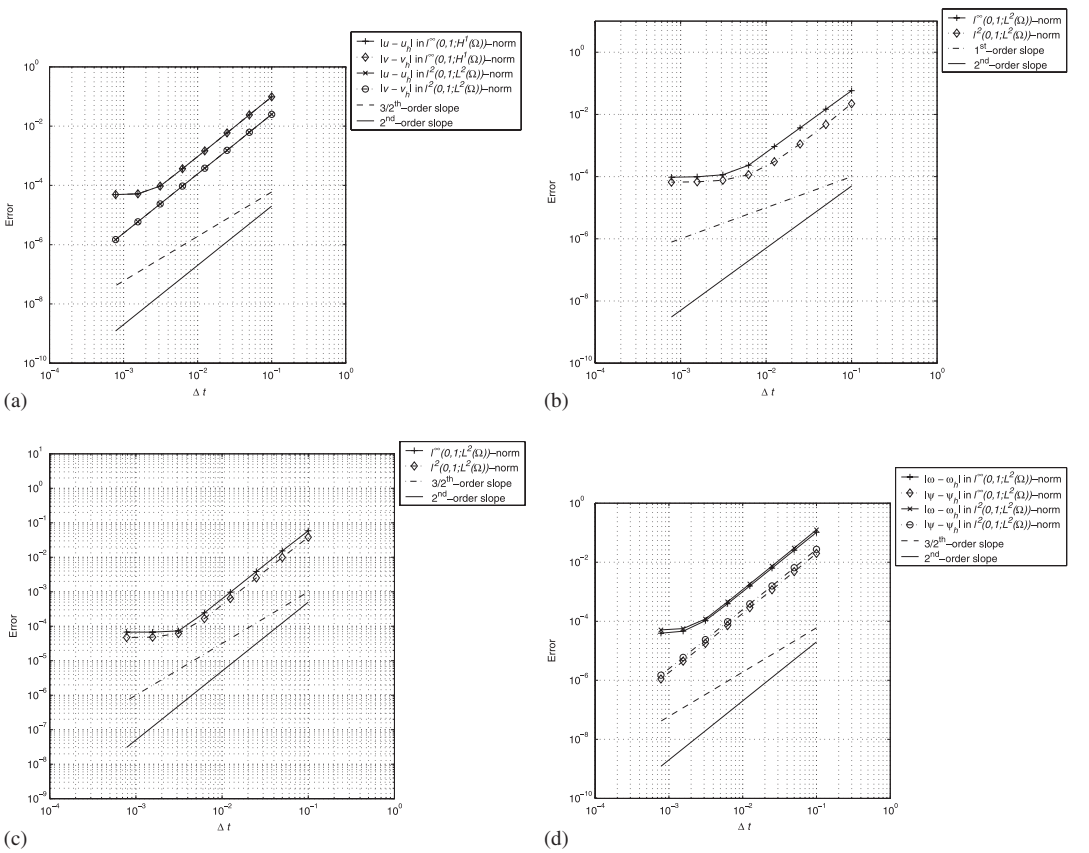

Figure 10. Convergence results for the velocity, pressure, divergence-free and vorticity/stream-function at $Re = 100$ and $T = 1$ using a pressure point boundary value: (a) velocity: 513×513 grid; (b) pressure: 257×257 grid; (c) divergence-free: 513×513 grid; and (d) velocity/stream-function: 513×513 grid.

pressure. For both primitive variables and vorticity/stream-function variables the convergence rate of the expected norm estimations is of second-order accuracy in time.

There is no noticeable difference between the $\mathbb{P}_2$ and the $\mathbb{P}_2/\mathbb{P}_1$ gradient matrix approximations, which are confirmed by the results given in Figures 4(f), 5(f), 6(f) and 7(f), and 9.

From these observations and others from various time-step sizes and mesh sizes, the scheme undoubtedly appears to be unconditionally stable.

4.1. *More numerical verifications*

Let us further examine the numerical accuracy of the approximate pressure. Does its scheme really perform a second-order accurate, $\mathcal{O}(\Delta t^2)$ in the $l^\infty(0, T; L^2(\Omega))$-norm?

Two analytical examples are considered here to illustrate the confirmation of the numerical codes developed for the present analysis. The exact solution of the problem Equations

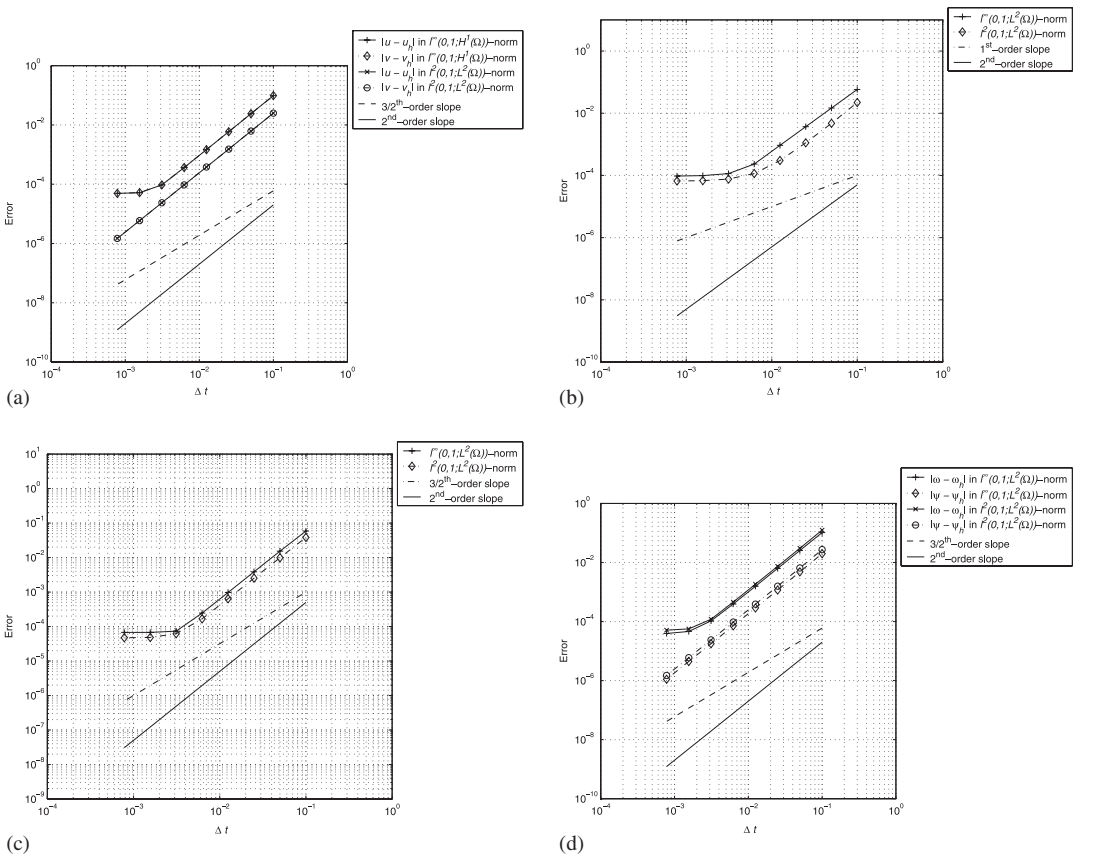

Figure 11. Convergence results for the velocity, pressure, divergence-free and vorticity/stream-function at $Re = 100$ and $T = 1$ using the augmented system: (a) velocity: 513×513 grid; (b) pressure: 257×257 grid; (c) divergence-free: 513×513 grid; and (d) vorticity/stream-function: 513×513 grid.

(1)–(2) on the square domain $\Omega = [-\pi/2, \pi/2]^2$ is chosen as follows [46]:

$$u(x, y, t) = -\cos(x)\sin(y)\sin(2t) \tag{46}$$

$$v(x, y, t) = \sin(x)\cos(y)\sin(2t) \tag{47}$$

$$p(x, y, t) = -\tfrac{1}{4}(\cos(2x) + \cos(2y))(\sin(2t))^2 \tag{48}$$

and the other example in $\Omega = [0, 1]^2$ is given in References [11, 13, 14] as follows:

$$u(x, y, t) = \pi\cos(2\pi y)\sin^2(\pi x)\sin(t) \tag{49}$$

$$v(x, y, t) = -\pi\sin(2\pi x)\sin^2(\pi y)\sin(t) \tag{50}$$

$$p(x, y, t) = \cos(\pi x)\sin(\pi y)\sin(t) \tag{51}$$

Due to space restrictions, for this paper, we only consider the boundary-refined mesh 513×513 for velocity, vorticity and stream-function, and 257×257 for the pressure. In the first run, the

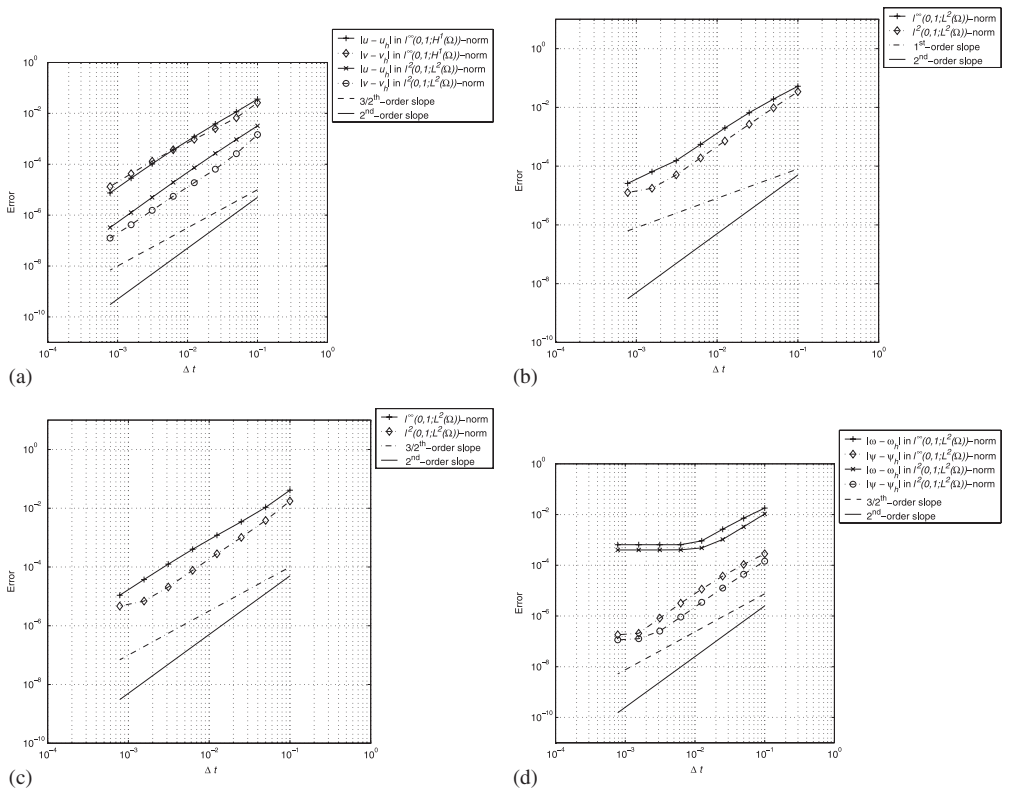

Figure 12. Convergence results for the velocity, pressure, divergence-free and vorticity/stream-function at $Re = 1$ and $T = 1$ using a pressure point boundary value: (a) velocity: 513×513 grid; (b) pressure: 257×257 grid; (c) divergence-free: 513×513 grid; and (d) vorticity/stream-function: 513×513 grid.

Reynolds number is set to 100, while in the second run, $Re = 1$. A selected final time is $T = 1$. The number of iterative steps for the estimation for the velocity, vorticity and stream-function is set to 14, 4 and 29, respectively, and for auxiliary pressure and pressure, is set to 22, and 4, respectively. The $\mathbb{P}_2$ gradient matrix is considered.

As indicated in Figures 10–13, convergence rate results of two test cases confirm that the approximate pressure is of $\mathcal{O}(\Delta t^2)$ in the $l^\infty(0, T; L^2(\Omega))$- and $l^2(0, T; L^2(\Omega))$-norms. Therefore, our findings coincide with Guermond and Shen's theoretical prediction.

5. NUMERICAL SIMULATIONS OF 2D DOUBLE LID-DRIVEN CAVITY PROBLEMS

The numerical simulations of 2D unsteady incompressible viscous flow in a double-lid driven cavity are presented in this section. Double lid-driven cavity problems are not as frequently

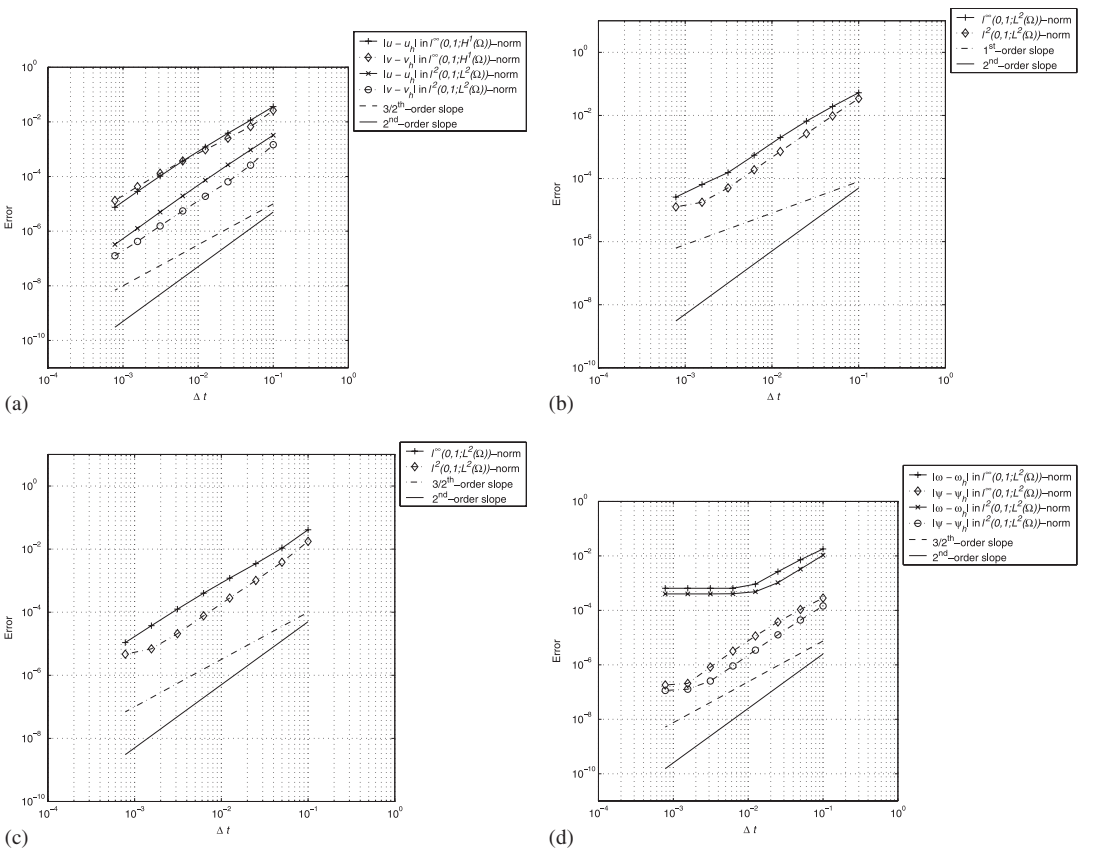

Figure 13. Convergence results for the velocity, pressure, divergence-free and vorticity/stream-function at $Re = 1$ and $T = 1$ using the augmented system: (a) velocity: 513×513 grid; (b) pressure: 257×257 grid; (c) divergence-free: 513×513 grid; and (d) vorticity/stream-function: 513×513 grid.

used as lid driven cavity problems for examining the performance of numerical schemes, but they share some similar features. For instance, the simplicity of the geometrical configuration of the cavity flow makes the problem handy to code, and easy to refine the mesh, apply boundary conditions, etc. Even though the problem setting looks simple in many aspects, the flow structure retains all the flow physics with counter rotating vortices located at the corners of the cavity. The change of flow pattern from a primary vortex to two primary vortices is observed. Interactions of physical mechanisms between primary vortices and corner eddies have not yet been fully explored. It is well-documented that the pattern of the pressure or pressure gradient is similar to the flow pattern of the velocity field. Three singularities that are located in the three corners where two moving walls meet two rigid walls and where the standard type of no-slip initial and boundary value conditions is assumed, are a unique characteristic of the double driven-lid cavity problems. Nevertheless, numerical inaccuracies of solutions still exist, like ripples, and propagate throughout the neighbourhood in two sharp positive and negative jumps, which cause unreliable qualitative information on eddy formation,

growth, separation, and reintegration into non-stationary flows. Full details on the lid-driven cavity topic are available in References [47, 48].

As discussed in Section 2, the pressure solution plus any arbitrary constant varying with the time is also, in concept, a solution of the pressure in the NS system. Any initial value for the pressure can be selected over the entire domain if the initial velocity is assumed to be zero. Unless otherwise mentioned, the results shown in this subsection were calculated from initial velocities and pressure of zero. Application of the augmented system for solving Equation (34) and use of the $\mathbb{P}_2$ gradient matrix approximation were performed in the work. The relative precision is set to 10^{-8}; the number of iteration for the all the computations is fixed at 200. The stream-function can be calculated *a posteriori* once the solution for the velocities has been obtained. By solving the Poisson equation, we have

$$\frac{\partial^2 \psi}{\partial x^2} + \frac{\partial^2 \psi}{\partial y^2} = \frac{\partial u}{\partial y} - \frac{\partial v}{\partial x} \tag{52}$$

subject to the boundary conditions $\psi|_{\partial\Omega} = 0$, and $\partial\psi/\partial n|_{\mathbf{x} \in \partial\Omega \setminus \partial\Omega'} = 0$ and $\partial\psi/\partial n|_{\mathbf{x} \in \partial\Omega'} = \pm 1$, where $\partial\Omega' = \partial\Omega_1 \cup \partial\Omega_2$ consists of $\partial\Omega_1$ and $\partial\Omega_2$, and stands for the part of $\partial\Omega$ with $\emptyset = \partial\Omega_1 \cap \partial\Omega_2$. Here, $\partial\Omega_1$ and $\partial\Omega_2$ specify the locations of the moving walls. The plus sign indicates the directions are moving from left to right, and from bottom to top.

5.1. The lids are moving from right to left and from top to bottom

The problem is the same as that used by Pan and Glowinski [15] and Ben-Artzi *et al.* [16] in recent studies of the 2D double lid-driven cavity flow. The following example is a version of 2D double lid-driven cavity flow defined on a unit domain $\Omega = [0, 1] \times [0, 1]$, with $\mathbf{f} = (0, 0)$. The associated boundary condition is given by

$$\begin{cases} u = v = 0 & \text{for } x = 0, \text{ or } y = 0 \\ u = -1, \quad v = 0 & \text{for } y = 1 \\ u = 0, \quad v = -1 & \text{for } x = 1 \end{cases} \tag{53}$$

The sketch in Figure 1 demonstrates the velocity boundary conditions. The mesh type was boundary-refined and the time step used was $\Delta t = 0.0005$ for $Re = 10\,000$.

Figures 14, 16–18 illustrate velocity vector field plots, and pressure, vorticity and stream-function contour plots. Figure 14 indicates that from $t = 2$ to 45, the birth and growth of a symmetric pair of cat's eye patterns are gradually induced by increasing the advection flow. By observing the figures, it can be seen that the line of symmetry is maintained as the time increases. The mechanism for the production and separation of small vortical cells from large ones along the 45° inclined centreline of the cavity is seen. A second mirror-symmetrical pair of counter-rotating cells appears at the lower left-hand corner. As the time increases, a third mirror-symmetrical pair of counter-rotating cells emerges at the upper right-hand corner.

No special treatment was considered to smooth out the corner singularities in this study. The Gibbs-like singularities of the pressure appeared at the double-lid velocity corners, as shown in Figure 15(a). Judging from the given figure, no boundary layer effect for the pressure along the given boundaries and no node-to-node pressure oscillations were made. To demonstrate the negligible effect on the internal feature of the pressure, except in the neighbourhood of the corner singularities, the following contour plots were cut down from the

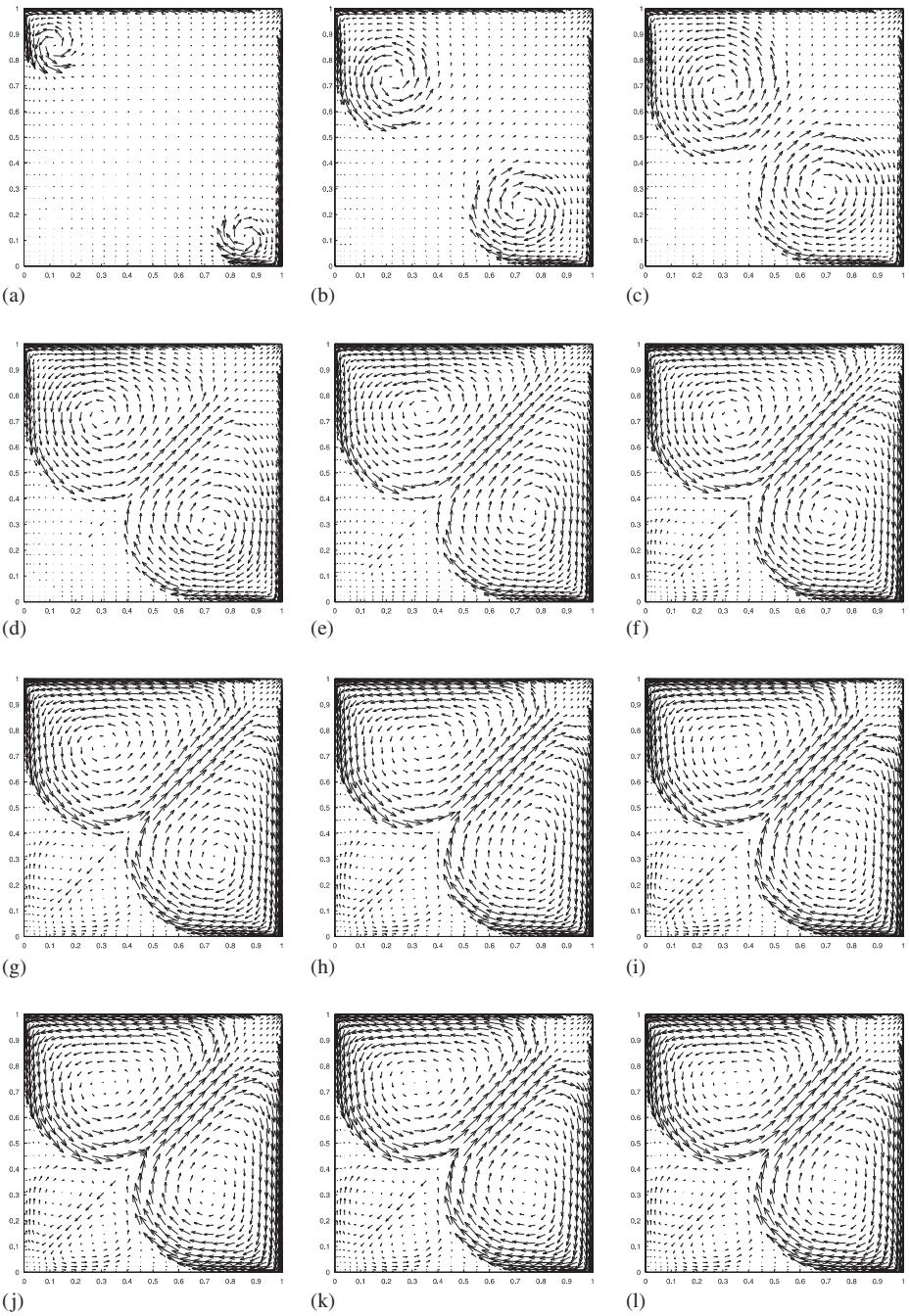

Figure 14. Time histories of velocity vector field plots. The lids are moving from right to left and from top to bottom. The mesh layout is 33×33: (a) $t = 2$; (b) $t = 6$; (c) $t = 10$; (d) $t = 14$; (e) $t = 18$; (f) $t = 22$; (g) $t = 26$; (h) $t = 30$; (i) $t = 34$; (j) $t = 38$; (k) $t = 42$; and (l) $t = 45$.

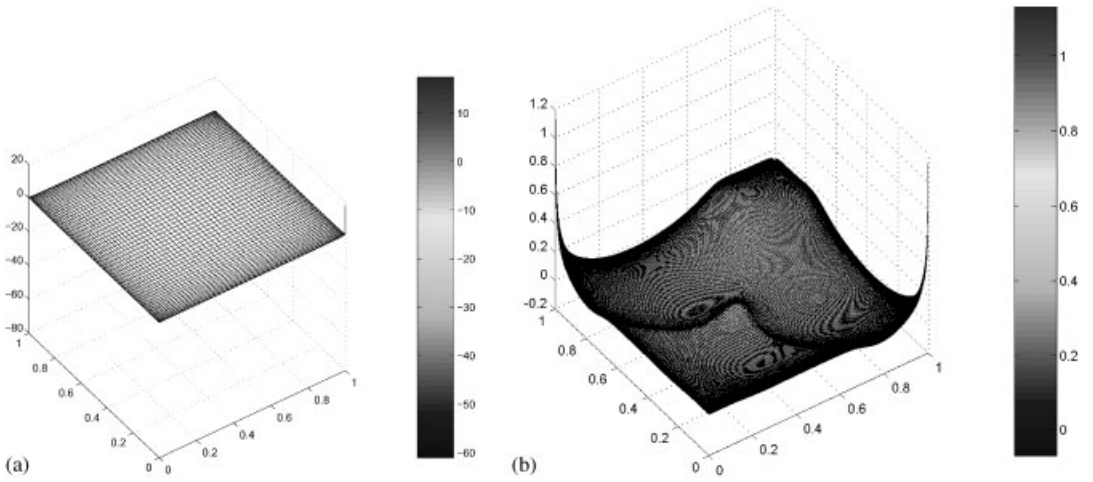

Figure 15. Mesh plots of pressure. The lids are moving from right to left and from top to bottom. The Reynolds number is $Re = 10\,000$. The mesh plot is shown for time $t = 46$. The mesh layout is 65×65 at the top page and 252×252 at the bottom page. The time step size is $\Delta t = 0.0005$.

actual size of computational grid, i.e. from 257×257 to 252×252. Until otherwise stated, all the pressure contour plots followed the same procedure. As shown in Figure 15(b), the pressure is influenced by the cavity corners. We observe in Figure 16 that the birth, growth and separation of mirror-symmetrical multi-pairs of pressure patterns remain.

As shown in Figure 17, emphasis is placed upon the structure of symmetrical vortex cells along the line of symmetry. As the time increases, a pair of elongated vortex cells induced by two counter-rotating cells at the lower left-hand corner pass through the axis, and move toward the upper right-hand corner. After hitting the corner, a pair of new counter-rotating vortex cells is formed. These small secondary and tertiary cells are competing a recirculation movement/direction again two main primary cells. As illustrated in Figure 17, up to $t = 45$, the presence of the symmetrical vortex patterns agrees with the numerical results produced by Ben-Artzi *et al.* [16]. Despite the numerical solutions of the vorticities/stream-functions that are obtained by the known velocity values at each time instant, mirror-symmetrical vortex results still remain, as shown in Figures 17 and 18.

5.2. The lids are moving from left to right and from bottom to top

Because there are no published results for this problem, a 2D double lid-driven cavity is simulated by letting $Re = 10\,000$. We consider $\Delta t = 0.0005$. The boundary-refined mesh layout of 513×513 grid was used. Velocity vector field plots, and vorticity, stream-function and pressure contour plots are shown in Figures 19–22, respectively, for various instants of non-dimensional time at $2, 6, 10, 14, 18$. From these plots we note that a vortex dipole gradually emerges from the right-hand corner, and the position of the vortex dipole shifts toward the lower left-hand corner. At $t = 10$, the separation and growth of a symmetric pair of two vortical structures remains. As the time increases, a second symmetric pair of two vortical structures gradually forms and grows. At $t = 18$, the symmetrical pattern along the 45° inclined

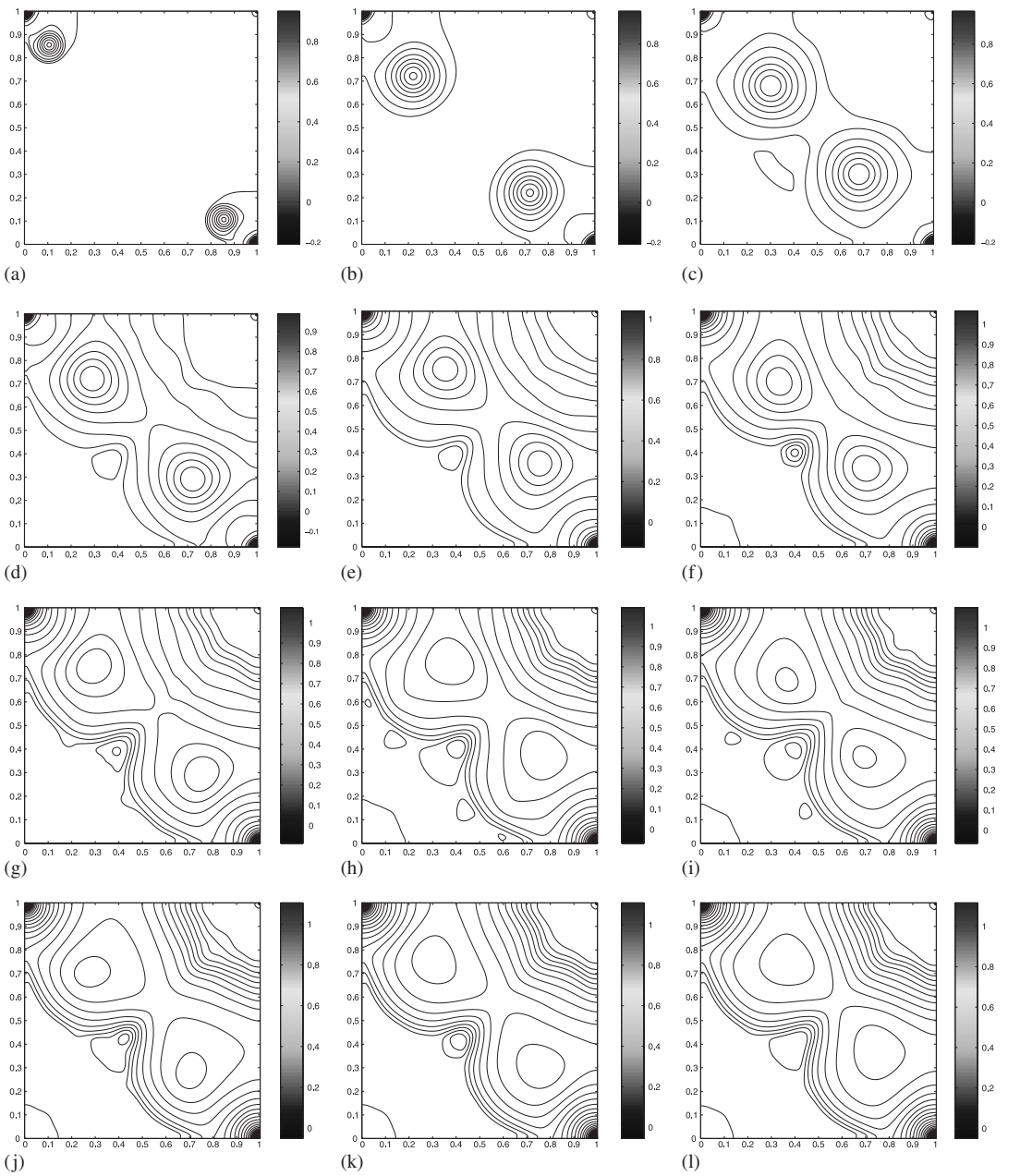

Figure 16. Time histories of pressure contours. The lids are moving from right to left and from top to bottom. The Reynolds number is $Re = 10\,000$. The mesh layout is 252×252 and the time step size is $\Delta t = 0.0005$: (a) $t = 2$; (b) $t = 6$; (c) $t = 10$; (d) $t = 14$; (e) $t = 18$; (f) $t = 22$; (g) $t = 26$; (h) $t = 30$; (i) $t = 34$; (j) $t = 38$; (k) $t = 42$; and (l) $t = 45$.

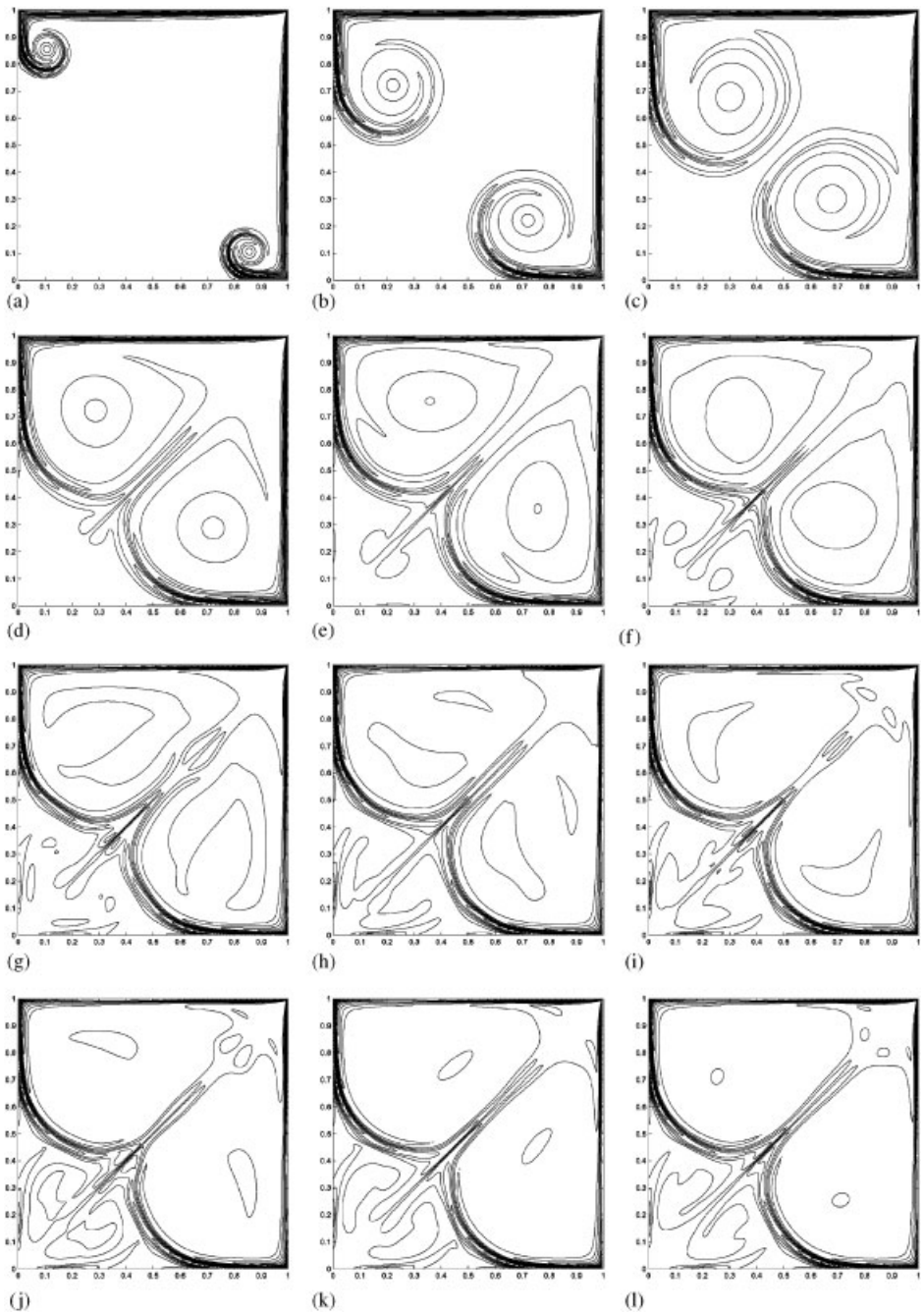

Figure 17. Time histories of vorticity contour plots. The lids are moving from right to left and from top to bottom. The mesh layout is 513×513: (a) $t = 2$; (b) $t = 6$; (c) $t = 10$; (d) $t = 14$; (e) $t = 18$; (f) $t = 22$; (g) $t = 26$; (h) $t = 30$; (i) $t = 34$; (j) $t = 38$; (k) $t = 42$; and (l) $t = 45$.

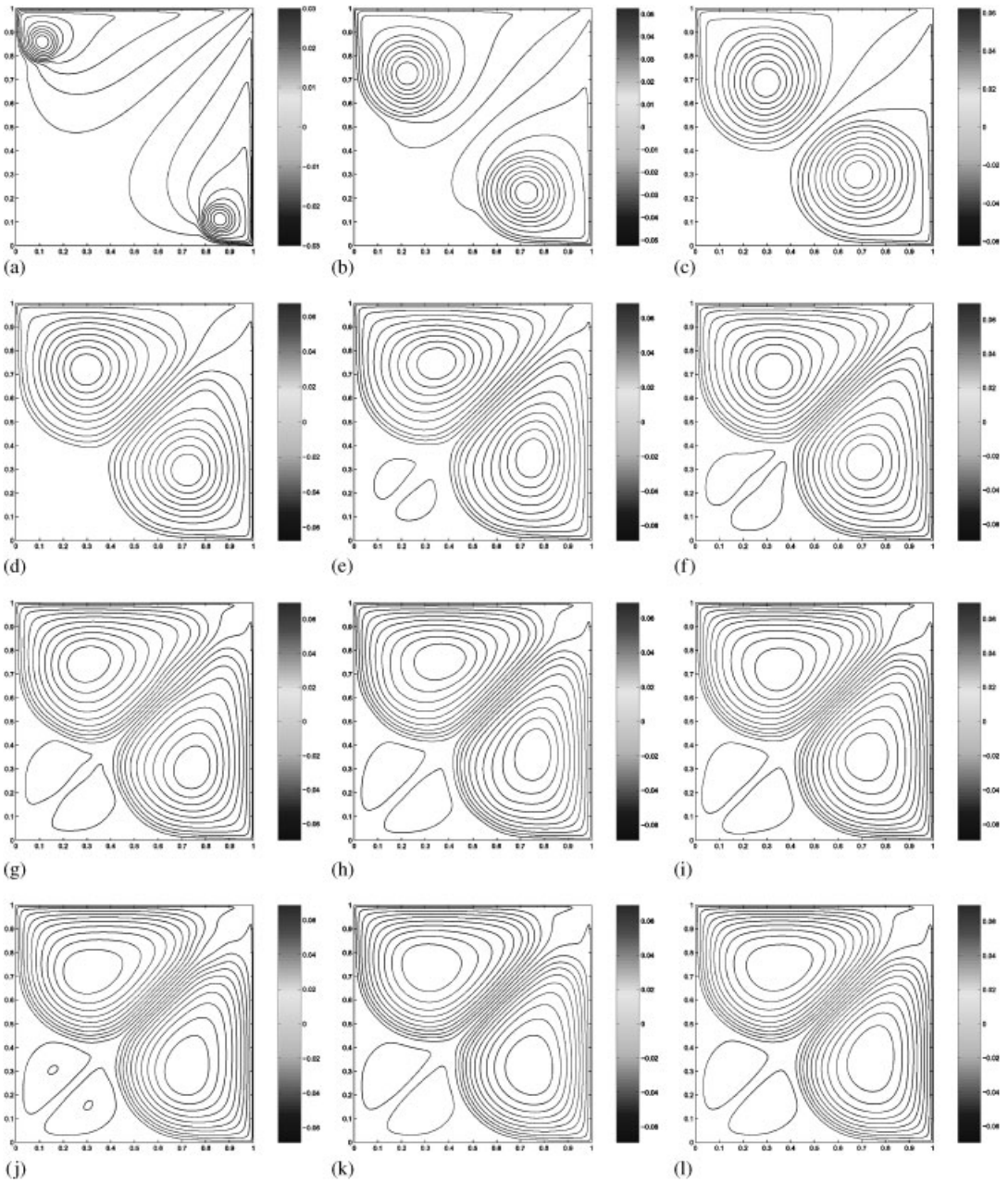

Figure 18. Time histories of stream-function contour plots. The lids are moving from right to left and from top to bottom. The Reynolds number is $Re = 10\,000$. The mesh layout is 513×513 and the time step size is $\Delta t = 0.0005$: (a) $t = 2$; (b) $t = 6$; (c) $t = 10$; (d) $t = 14$; (e) $t = 18$; (f) $t = 22$; (g) $t = 26$; (h) $t = 30$; (i) $t = 34$; (j) $t = 38$; (k) $t = 42$; and (l) $t = 45$.

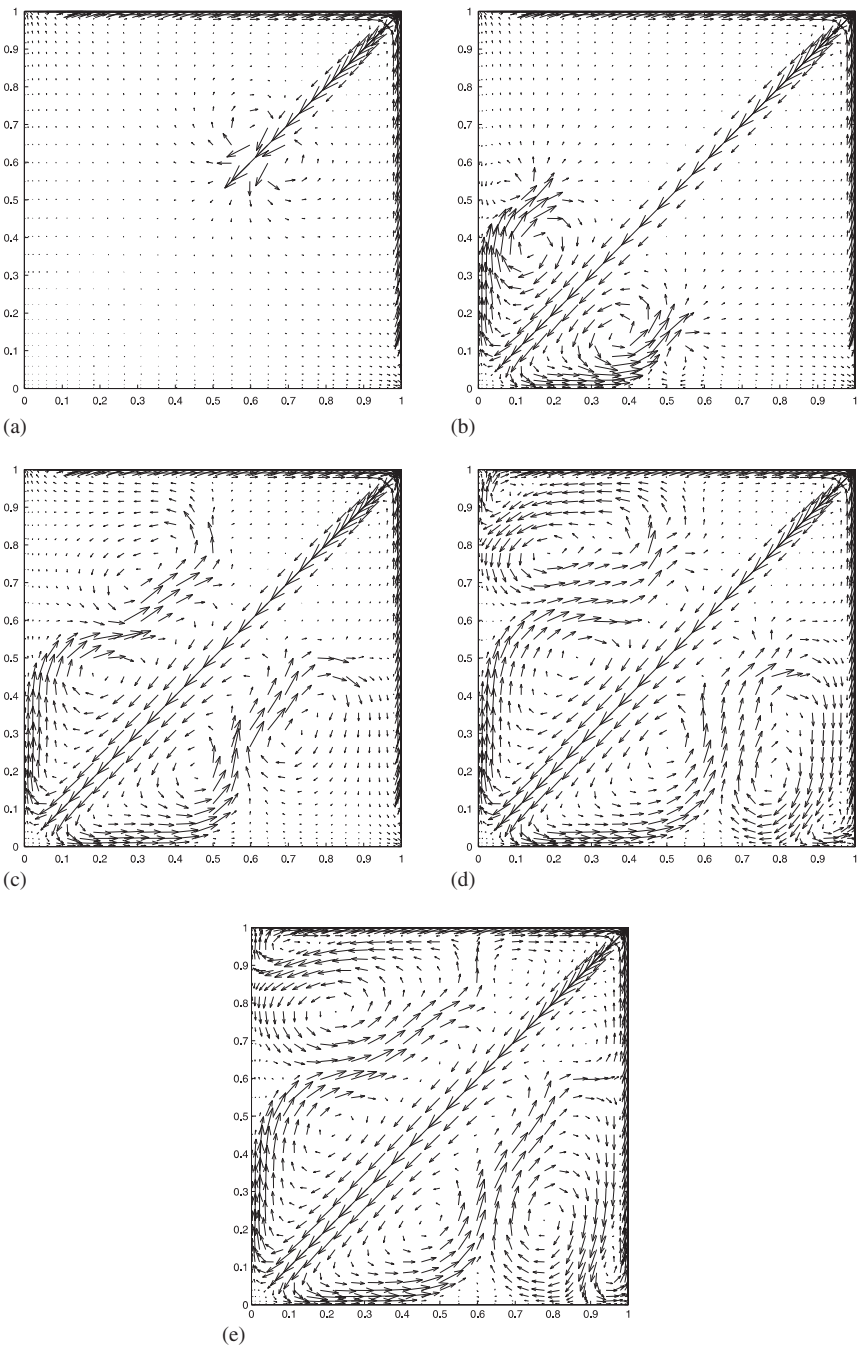

Figure 19. Time histories of velocity vector field plots. The lids are moving from left to right and from bottom to top. The Reynolds number is $Re = 10\,000$. The contours are shown for time $t = 2, 6, 10, 14,$ and 18. The mesh layout is 33×33 and the time step size is $\Delta t = 0.0005$.

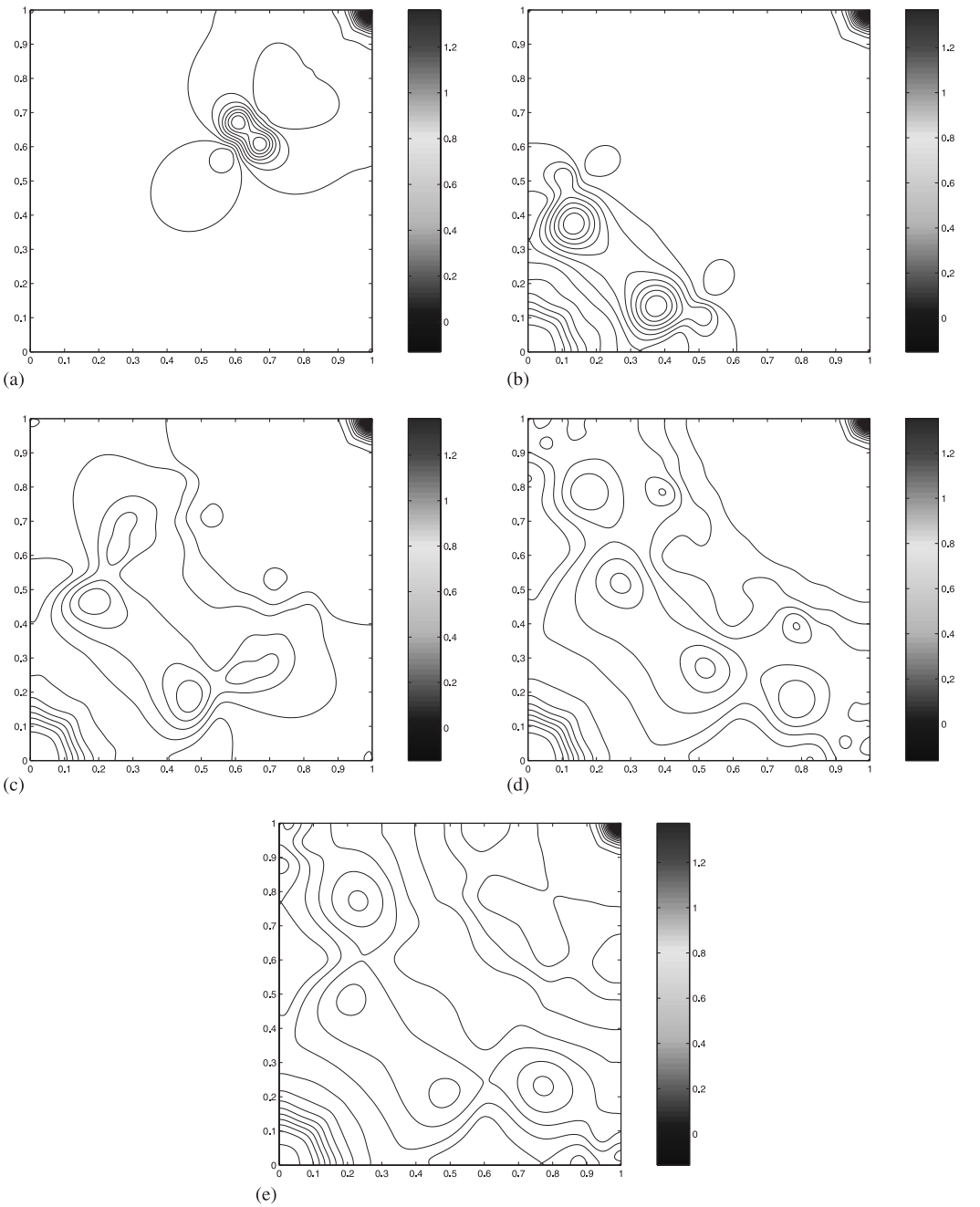

Figure 20. Time histories of pressure contour plots. The lids are moving from left to right and from bottom to top. The Reynolds number is $Re = 10\,000$. The contours are shown for time $t = 2, 6, 10, 14,$ and 18. The mesh layout is 252×252 and the time step size is $\Delta t = 0.0005$.

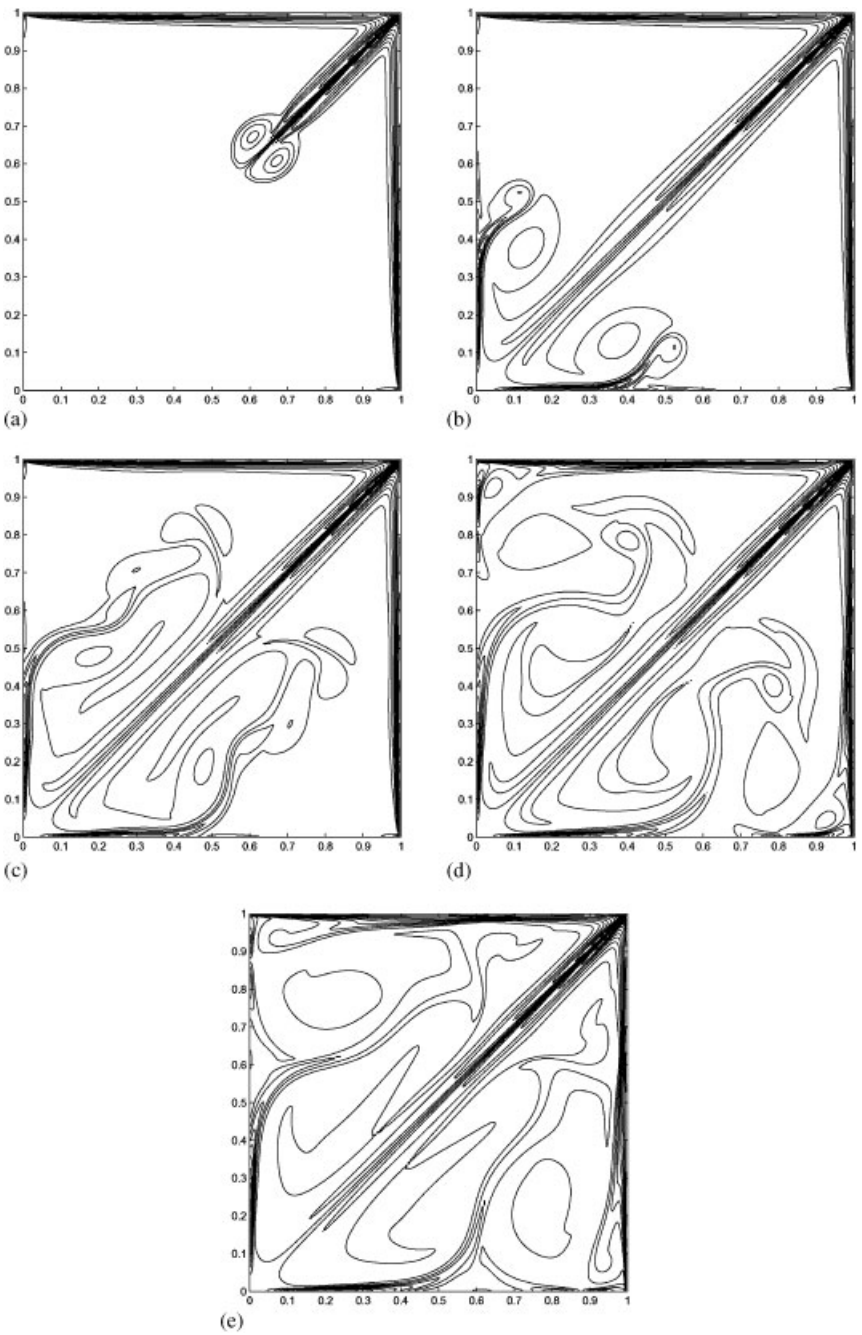

Figure 21. Time histories of vorticity contour plots. The lids are moving from left to right and from bottom to top. The Reynolds number is $Re = 10\,000$. The contours are shown for time $t = 2, 6, 10, 14,$ and 18. The mesh layout is 257×257 and the time step size is $\Delta t = 0.0005$.

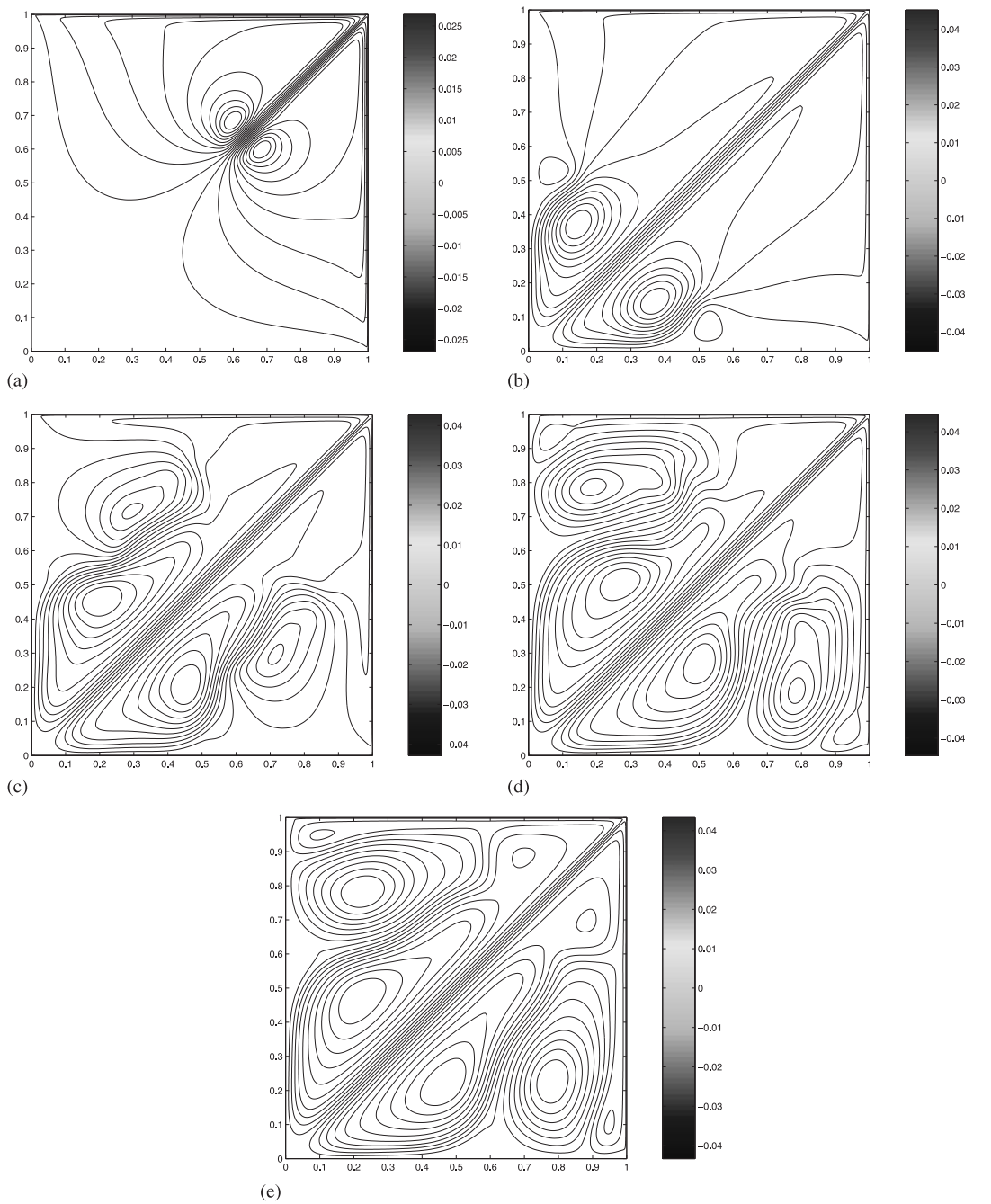

Figure 22. Time histories of stream-function contour plots. The lids are moving from left to right and from bottom to top. The Reynolds number is $Re = 10\,000$. The contours are shown for time $t = 2, 6, 10, 14,$ and 18. The mesh layout is 513×513 and the time step size is $\Delta t = 0.0005$.

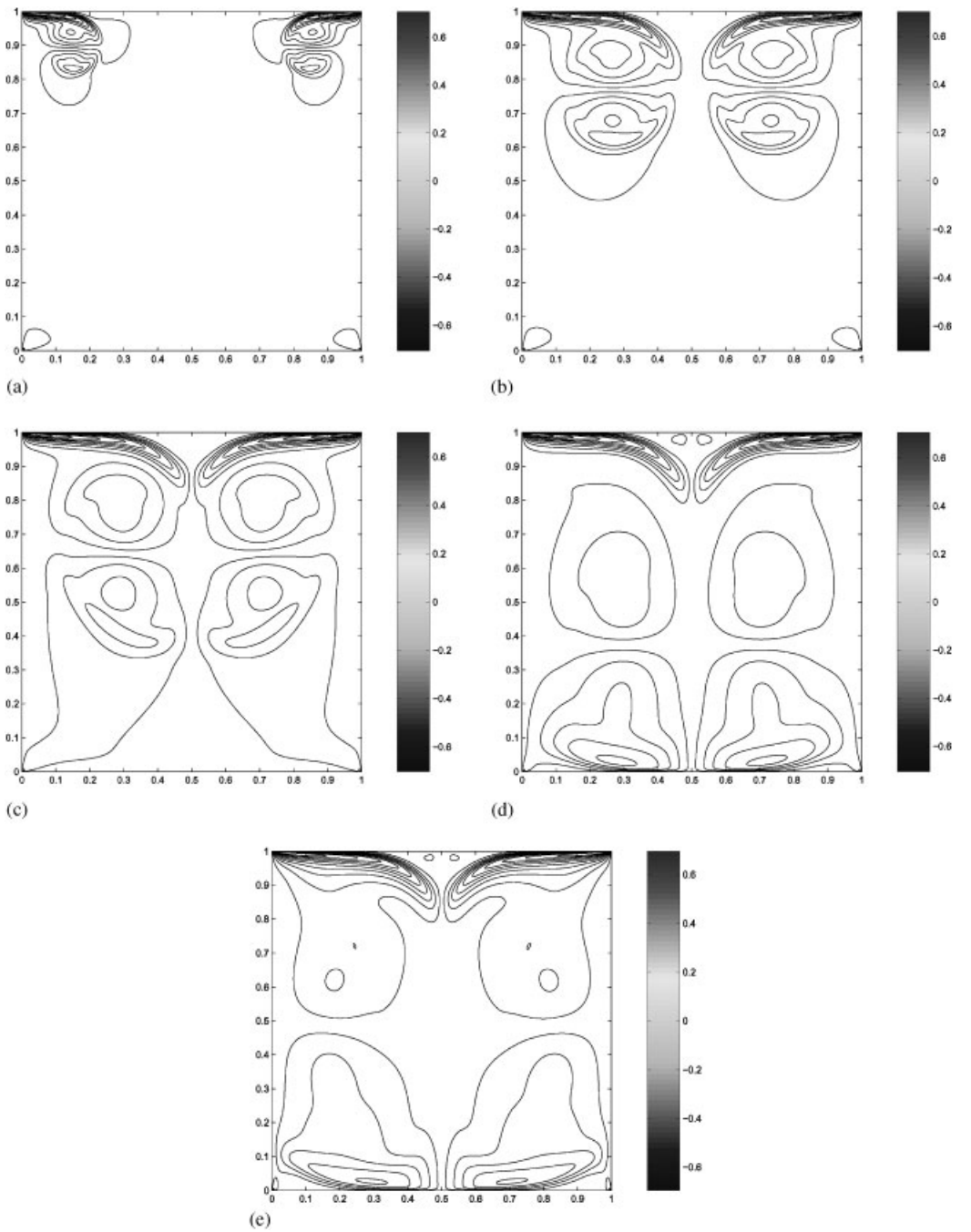

Figure 23. Contour plots of u-velocity component. The left- and right-hand lids are moving in the same direction from bottom to top. The Reynolds number is $Re = 10\,000$. The contours are shown for time $t = 2, 6, 10, 14$, and 18. The mesh layout is 513×513 and the time step size is $\Delta t = 0.0005$.

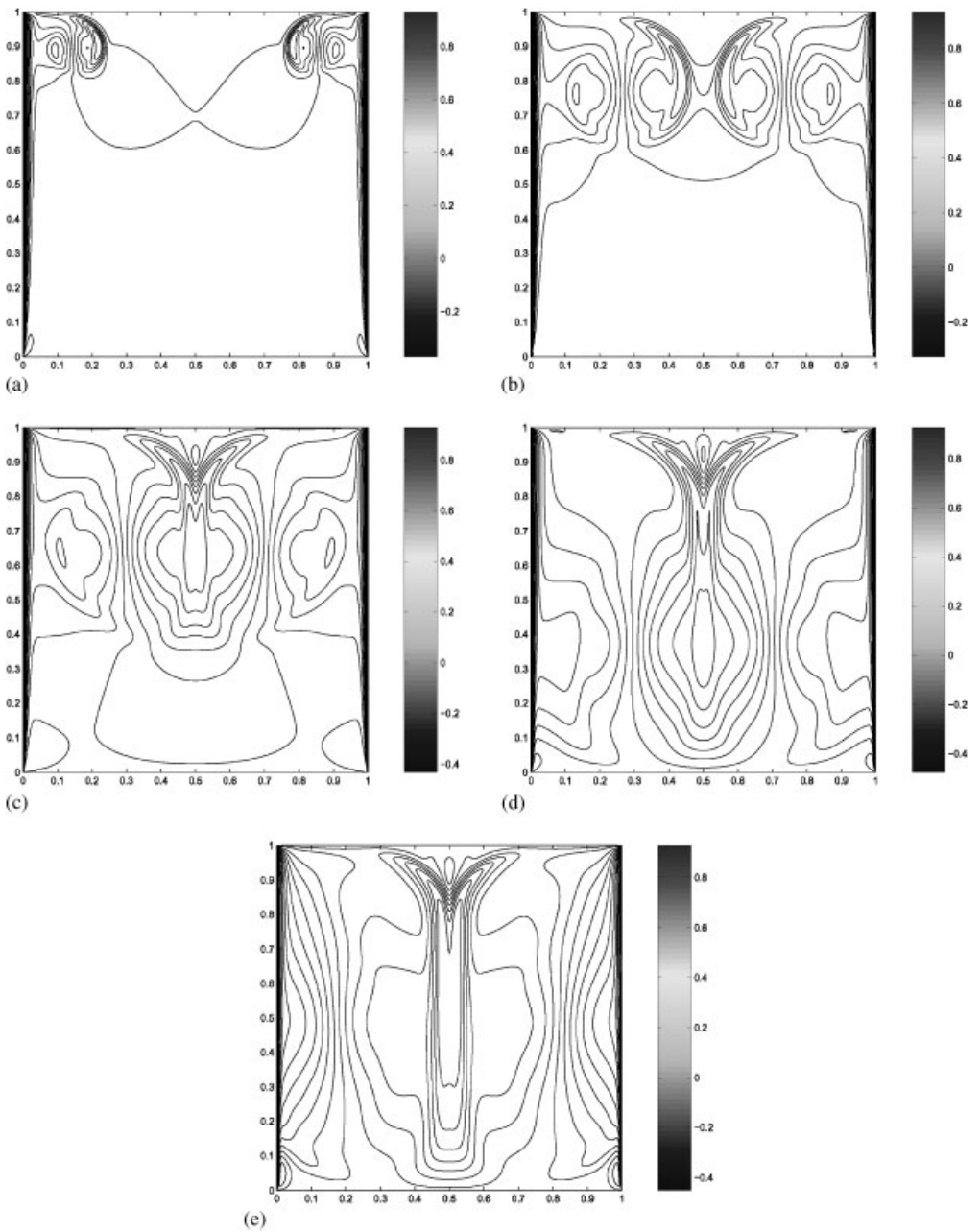

Figure 24. Contour plots of v-velocity component. The left- and right-hand lids are moving in the same direction from bottom to top. The Reynolds number is $Re = 10\,000$. The contours are shown for time $t = 2, 6, 10, 14,$ and 18. The mesh layout is 513×513 and the time step size is $\Delta t = 0.0005$.

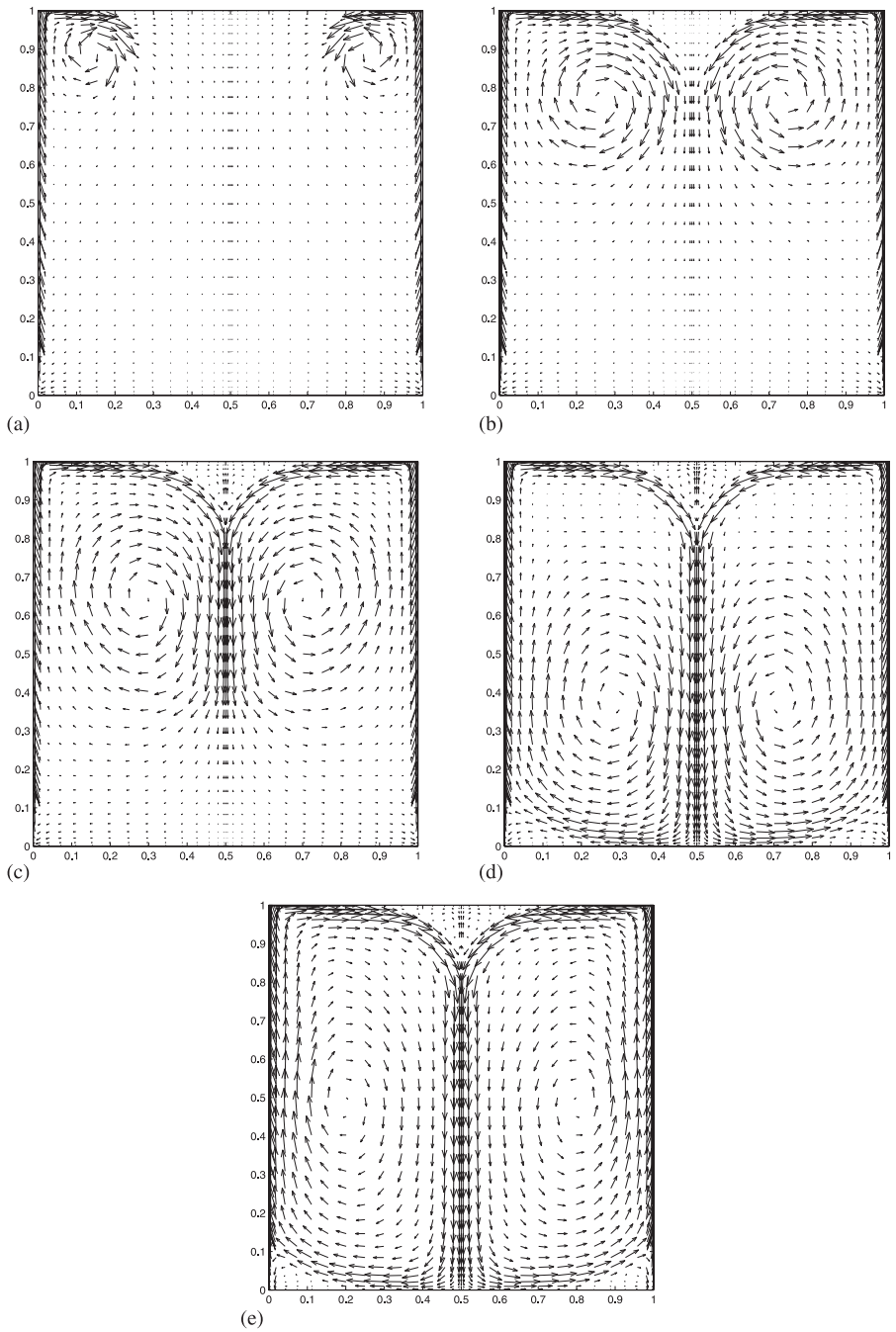

Figure 25. Time histories of velocity vector field plots. The left- and right-hand lids are moving in the same direction from bottom to top. The Reynolds number is $Re = 10\,000$. The contours are shown for time $t = 2, 6, 10, 14$, and 18. The mesh layout is 33×33 and the time step size is $\Delta t = 0.0005$.

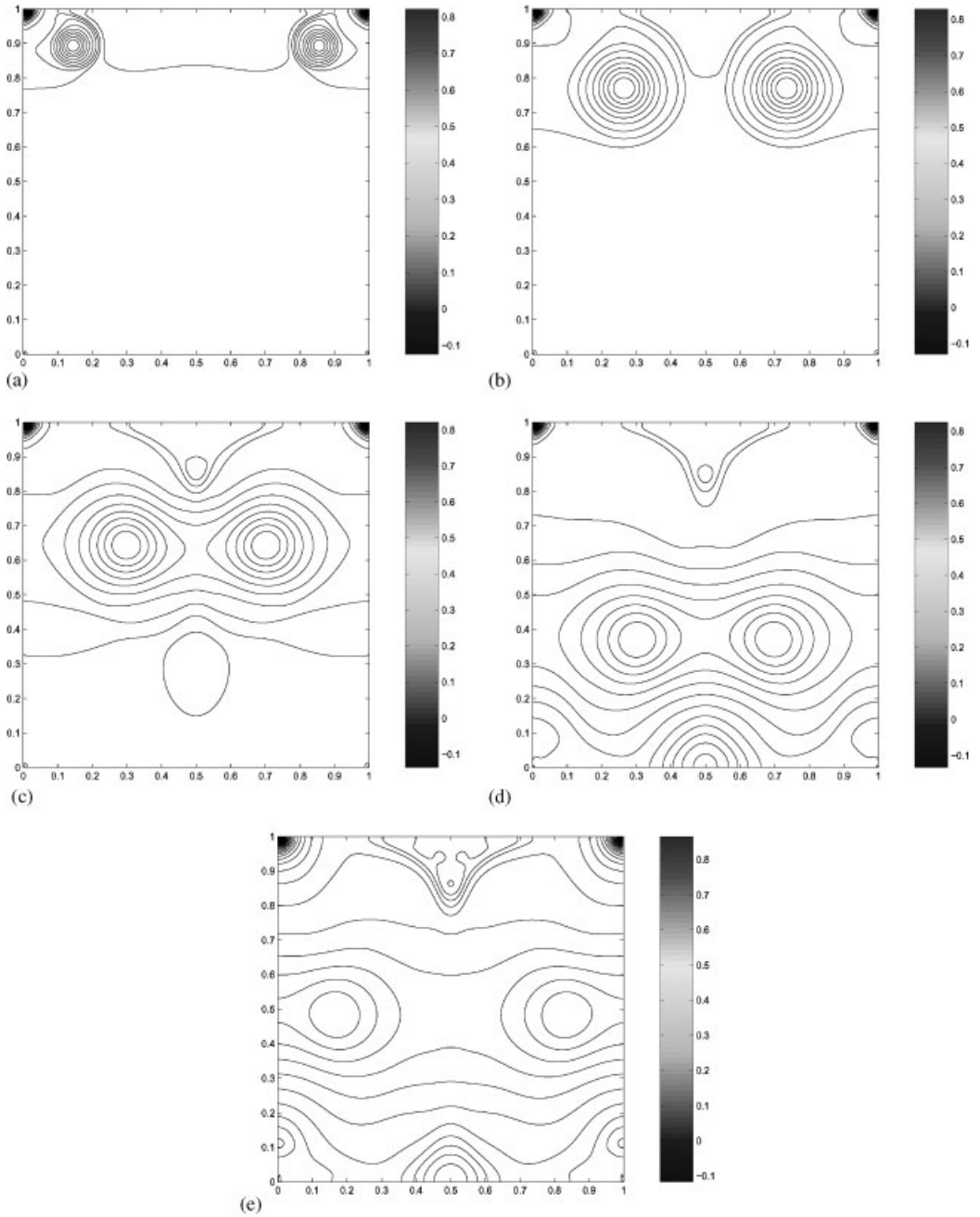

Figure 26. Time histories of pressure contour plots. The left- and right-hand lids are moving in the same direction from bottom to top. The Reynolds number is $Re = 10\,000$. The contours are shown for time $t = 2, 6, 10, 14$, and 18. The mesh layout is 252×252 and the time step size is $\Delta t = 0.0005$.

centreline of the cavity remains unchanged. A third symmetric pair of two vortical structures gradually emerges from the upper left-hand corner and lower right-hand corner.

5.3. *The left- and right-hand lids are moving in the same direction from bottom to top*

The problem is the same as that used by Kupferman [18] in a recent study of the 2D double lid-driven cavity flow. Instead of examining $Re = 20\,000$, we use $Re = 10\,000$. The two cell boundary-refined mesh layout with the 513×513 grid is used. We consider $\Delta t = 0.0005$. The main goal of our investigation is to discover the symmetry-preserving mechanism on the flow field. Owing to the symmetrical boundary conditions for the v-component velocity on the vertical walls, the flow and pressure fields perform a symmetrical pattern formulation, as shown in Figures 23, 24, and 26. Because of the symmetry, the vector flow fields in the right and left halves of the cavity are identical, as shown in Figure 25. We find from all these figures that the evolution of the two symmetrical patterns gradually grows as the time increases. From the results displayed in Figures 25 and 26, we see that the pattern of the velocity vector field plots is similar to that of the pressure contour plots. As can be seen from Figure 25, at $t = 2$ the birth and growth of a single cat's eye emerges from both the right- and left-hand sides of the top corner. From $t = 2$ to 6, the two symmetrical flow fields begin interacting with each other. At $t = 10$, the two cat's eyes collide with each other and move downward. A mirror-symmetric pair of two counter-rotating cells gradually appears at the mid-plane of the top cavity. As time goes on, the intensity of the recirculation increases. At $t = 14$, a third symmetrical pair of two counter-rotating cells gradually emerges from the lower left- and right-hand corners. At $t = 18$, two symmetrical flow fields hit the bottom wall and rebound upward.

6. CONCLUDING REMARKS

The mathematical model proposed by Guermond and Shen [11] and the computer algorithm developed in this investigation appear to be suitable for the computation of the 2D double driven-lid cavity flows. For moderate Reynolds numbers, two sliding lids produced a 2D motion at a fixed time interval in agreement with the literature. Despite the large set of the finite grid used, the change of flow pattern from bicellular to multicellular is observed. A series plot of velocity vector fields, and pressure, vorticity and stream-function contours appears to be useful for illustrating symmetrical pairs of multicellular structures.

Our past experience indicated that for double-lid cavity problems, the deterioration in the structure of a symmetric flow happened due to the improper choices of the time step size and grid size, the effect of mesh layout, the treatment of the singular corners, and the choice of the initial values for the pressure. It was shown that it is feasible to improve the axis of symmetry under appropriate conditions: if a small time-step size is taken and the boundary-refined grid is used with greater resolution near the boundaries [49]. Further investigation of this work could include the long time behaviour of the unsteady vortex structure, the occurrence of the Hopf bifurcation, the cause of the symmetry-breaking and the special treatment of the non-linear term. These topics will be presented in a separate study.

ACKNOWLEDGEMENTS

The authors would like to acknowledge the encouragement and helpful suggestions from Prof. Jun Zou. They would like to express our appreciation to Frank Ng for help with the computing facility. The computations were performed on the IBM RS/6000 SP system at the Chinese University of Hong Kong. The authors would like to thank the reviewers for careful reading of the manuscript and valuable suggestions.

REFERENCES

1. Chorin AJ. Numerical solution of the Navier–Stokes equations. *Mathematics of Computation* 1968; **22**:745–762.
2. Chorin AJ. On the convergence of discrete approximations to the Navier–Stokes equations. *Mathematics of Computation* 1969; **23**:341–353.
3. Témam R. Sur l'approximation de la solution des équations de Navier–Stokes par la méthode des pas fractionnaires. I. *Archive for Rational Mechanics and Analysis* 1969; **32**:135–153 (in French).
4. Témam R. Sur l'approximation de la solution des équations de Navier–Stokes par la méthode des pas fractionnaires. II. *Archive for Rational Mechanics and Analysis* 1969; **33**:377–385 (in French).
5. Gresho P, Sani R, Engelman MS. *Incompressible Flow and the Finite Element Method Advection–Diffusion and Isothermal Laminar Flow*. Wiley: West Sussex, U.K., 1998.
6. Deville MO, Fischer PF, Mund EH. *Higher Order Methods for Incompressible Fluid Flow*. Cambridge University Press: Cambridge, MA, 2002.
7. Donea J, Huerta A. *Finite Element Methods for Flow Problems*. Wiley: Chichester, Hoboken, NJ, 2003.
8. Glowinski R. Finite element methods for incompressible viscous flow. In *Handbook of Numerical Analysis*, Ciarlet PG, Lions JL (eds). Elsevier/North-Holland: Amsterdam, 2003.
9. Ern A, Guermond JL. *Theory and Practice of Finite Elements*. Applied Mathematical Sciences, vol. 159. Springer: New York, 2004.
10. Guermond JL, Minev P, Shen J. An overview of projection methods for incompressible flows. *Computer Methods in Applied Mechanics and Engineering* 2005, in press.
11. Guermond JL, Shen J. A new class of truly consistent splitting schemes for incompressible flows. *Journal of Computational Physics* 2003; **192**:262–276.
12. Guermond JL, Shen J. Quelques résultats nouveaux sur les méthodes de projection (New results on several projection methods). *Comptes Rendus de l'Académie des Sciences*, *Série I*, *Mathématique* 2001; **333**: 1111–1116 (in French).
13. Guermond JL, Shen J. Velocity-correction projection methods for incompressible flows. *SIAM Journal on Numerical Analysis* 2003; **41**:112–134.
14. Guermond JL, Shen J. On the error estimates for the rotational pressure-correction projection methods. *Mathematics of Computation* 2004; **73**:1719–1737.
15. Pan TW, Glowinski R. A projection/wave-like equation method for the numerical simulation of incompressible viscous fluid flow modeled by the Navier–Stokes equations. *Computational Fluid Dynamics Journal* 2000; **9**:28–42.
16. Ben-Artzi M, Fishelov D, Trachtenberg S. Vorticity dynamics and numerical resolution of Navier–Stokes equations. *Mathematical Modelling and Numerical Analysis* 2001; **35**(2):313–330.
17. Ben-Artzi M, Croisill JP, Fishelov D, Trachtenberg S. A pure-compact scheme for the streamfunction formulation of Navier–Stokes equations. *Journal of Computational Physics* 2005; **205**:640–664.
18. Kupferman R. A central-difference scheme for a pure stream function formulation of incompressible viscous flow. *SIAM Journal on Scientific Computing* 2001; **23**(1):1–18.
19. Kurganov A, Tadmor E. New high-resolution semi-discrete central schemes for Hamilton–Jacobi equations. *Journal of Computational Physics* 2000; **160**(2):720–742.
20. Altas I, Dym J, Gupta MM, Manohar RP. Multigrid solution of automatically generated high-order discretizations for the biharmonic equation. *SIAM Journal on Scientific Computing* 1998; **19**(5):1575–1585.
21. Kickinger K. Algebraic multi-grid for discrete elliptic second-order problems (English summary). In *Multigrid Methods V* (*Stuttgart*, 1996), Pavarino L, Toselli A (eds), Lecture Notes in Computational Science and Engineering, vol. 3. Springer: Berlin, 1998; 157–172.
22. Quartapelle L. *Numerical Solutions of the Incompressible Navier–Stokes Equations*. Birkhäuser: Basel, 1994.
23. Ladyžhenskaya OA. *Mathematical Problems in the Dynamics of a Viscous Incompressible Flow*. Gordon & Breach: New York, 1963.
24. Ladyžhenskaya OA. Mathematical analysis of Navier–Stokes equations for incompressible liquids. *Annual Review of Fluid Mechanics* 1975; **7**:249–272.

25. Timmermans LJP, Minev PD, Van De Vosse FN. An approximate projection scheme for incompressible flow using spectral elements. *International Journal for Numerical Methods in Fluids* 1996; **22**:673–688.
26. Goda K. A multistep technique for the with implicit difference schemes for calculating two- or three-dimensional cavity flows. *Journal of Computational Physics* 1979; **30**:76–95.
27. Turek S. A comparative study of time-stepping techniques for the incompressible Navier–Stokes equations: from fully implicit non-linear schemes to semi-implicit projection methods. *International Journal for Numerical Methods in Fluids* 1996; **22**:987–1011.
28. Quarteroni A, Valli A. *Numerical Approximation of Partial Differential Equations*. Springer Series in Computational Mathematics, vol. 23. Springer: Berlin, 1994.
29. Shen J. On error estimates of some higher order projection and penalty-projection methods for Navier–Stokes equations. *Numerische Mathematik* 1992; **62**(1):49–73.
30. Kellogg OD. *Foundations of Potential Theory*. Springer: Berlin, 1929.
31. Lighthill MJ. Introduction—boundary layer theory. In *Laminar Boundary Layers*: *An Account of the Development*, *Structure*, *and Stability of Laminar Boundary Layers in Incompressible Fluids*, Rosenhead L (ed.). Oxford Engineering/Clarendon Press: New York, 1963; 46–109.
32. Chu CK. Numerical methods in fluid dynamics. *Advances in Applied Mechanics* 1978; **18**:285–331.
33. Gresho P, Lee RL, Sani R. On the time-dependent solution of the incompressible Navier–Stokes equations in two and three dimensions. In *Recent Advances in Numerical Methods in Fluids*: *Volume 1*, Taylor C, Morgan K (eds). Prineridge: Swansea, 1980; 27–79.
34. Donea J, Giuliani S, Laval H, Quartapelle L. Solution of the unsteady Navier–Stokes equations by a finite-element projection method. In *Recent Advances in Numerical Methods in Fluids*: *Volume 2*, Taylor C, Morgan K (eds). Prineridge: Swansea, 1981; 97–132.
35. Girault V, Raviart P. *Finite Element Approximation of the Navier–Stokes Equations*. Springer: New York, 1981.
36. Brezzi F, Fortin M. *Mixed and Hybrid Finite Element Methods*. Springer: Berlin, Heidelberg, 1991.
37. Saad Y. SPARSKIT: a basic tool-kit for sparse matrix computations (Version 2). http://www.users.cs.umn.edu/∼saad/software/SPARSKIT/sparskit.html
38. Henshaw WD, Petersson NA. A split-step scheme for the incompressible Navier–Stokes equations. In *Numerical Solutions of Incompressible Flows*, Hafez MM (ed.). World Scientific Publishing Company: Singapore, 2003; 108–125.
39. Pearson CE. A computational method for time dependent two dimensional incompressible viscous flow problems. *Rep. SRRC-RR-64-17*, Sperry Rand Research Center, Sudbury, MA, 1964.
40. Braza M, Chassaing P, Ha Minh H. Numerical study and physical analysis of the pressure and velocity fields in the near wake of a circular cylinder. *Journal of Fluid Mechanics* 1986; **165**:79–130.
41. Mansutti D, Graziani G, Piva R. A discrete vector potential model for unsteady incompressible viscous flows. *Journal of Computational Physics* 1991; **92**:161–184.
42. Strikwerda JC. High-order accurate schemes for incompressible viscous flow. *International Journal for Numerical Methods in Fluids* 1994; **24**:715–734.
43. Taylor GI. On the decay of vortices in a viscous fluid. *Philosophical Magazine* 1923; **46**:671–674.
44. Ethier CR, Steinman DA. Exact fully 3D Navier–Stokes solutions for benchmarking. *International Journal for Numerical Methods in Fluids* 1994; **19**:369–375.
45. Gervais JJ, Lemelin D, Pierre R. Some experiments with stability analysis of discrete incompressible flows in the lid-driven cavity. *International Journal for Numerical Methods in Fluids* 1997; **24**:477–492.
46. Guermond JL, Quartapelle L. On stability and convergence of projection methods based on pressure Poisson equation. *International Journal for Numerical Methods in Fluids* 1998; **26**:1039–1053.
47. Gustafson K. Four principles of vortex motion. In *Vortex Methods and Vortex Motion*, Gustafson KE, Sethian JA (eds). SIAM: Philadelphia, 1991; 95–141.
48. Shankar PN, Deshpande MD. Fluid mechanics in the driven cavity. *Annual Review of Fluid Mechanics* 2000; **32**:93–136.
49. Wong CF. Numerical studies of projection methods. *Ph.D. Thesis*, Department of Mathematics, Chinese University of Hong Kong, 2004.

